Petrophysical Characterization of Metamorphic Rocks using X-ray Micro-CT data – Implications for fluid flow

Ritwik Chakraborty [a,*], Michael Späth [b], Akash Kumar [b], Benjamin Busch [c], Britta Nestler [b,d], Manish A. Mamtani [a], Christoph Hilgers [c]

[a] Department of Geology and Geophysics, Indian Institute of Technology, Kharagpur, 721302, India
[b] Institute of Nanotechnology (INT-MSS), Karlsruhe Institute of Technology (KIT), Hermann-von-Helmholtz-Platz 1, 76344, Eggenstein-Leopoldshafen, Germany
[c] Institute of Applied Geosciences (Structural Geology & Tectonics), Karlsruhe Institute of Technology, Adenauerring 20a, 76131, Karlsruhe, Germany
[d] Institute for Applied Materials (IAM-MMS), Karlsruhe Institute of Technology, Strasse Am Forum 7, 76131, Karlsruhe, Germany

Keywords:
Porosity
Permeability
X-ray micro-CT
Metamorphic rocks
Threshold
Multiphase-field

A B S T R A C T

The petrophysical properties (porosity and permeability) of rocks are significantly influenced by their microstructure and fabric anisotropy, which can be evaluated using X-ray micro-computed tomography (μCT). Through study of mica schists from the Singhbhum Shear Zone (Eastern India), we demonstrate the potential to perform X-ray micro-CT studies in metamorphic rocks and discuss the associated challenges in data processing. We show that automated thresholding of greyscale values from μCT data acquisition yields abnormally high porosity/permeability values in schists when compared to the values obtained from laboratory measurements of the same samples. We develop a *modus operandi* where the laboratory measured porosity value from an individual schist sample is used to calibrate the greyscale threshold range (designating void space) of μCT data from the same sample. This calibration is done using PACE3D numerical simulation framework that allows a multiphase-field approach, and it is shown that (a) porosities of schist derived from analysis of μCT data (post re-thresholding) fit well with laboratory measured values of respective samples and (b) anisotropy of permeability can be computed from μCT data. Permeability computed using the μCT data (post re-thresholding) vis-à-vis laboratory measurements are comparable in 4 out of 5 schist samples analysed here, when the samples are treated as a two phase system (void spaces as one phase and solid rock mass as the second phase) in PACE3D. The aberration in one schist sample is attributed to its heterogeneous layering and microstructure that comprises alternate layers of coarse and fine grain size aggregates of phyllosilicate + quartz. Re-computation of permeability by performing three-phase simulations for the above layered sample in PACE3D framework by introducing phyllosilicate as a third phase (in addition to void spaces and other mineral phases) yields results similar to the laboratory measurements. We conclude that our approach of integrating μCT data, laboratory measurement of petrophysical properties and microstructure modelling/simulation in PACE3D multiphase-field framework helps evaluate the role of rheological variations in controlling porosity/permeability. Thus this study has a bearing on enhancing knowledge about fluid flow in metamorphic rocks with possible implications for mineralization.

1. Introduction

X-ray micro-computed tomography (commonly referred to as micro-CT/μCT) is a non-destructive technique for investigating the internal structure and properties of a material typically on the order of micrometres to millimetres. In geosciences, it has emerged as a powerful imaging technique that allows researchers to acquire high-resolution images of rock samples for 3D visualization of microstructure and analysis of petrophysical properties such as porosity, permeability and tortuosity (Mees et al., 2003; Callow et al., 2020).

In the past few decades there has been a particular focus on the study of sedimentary rocks with μCT, especially with regards to the analysis of complex pore networks in reservoir rocks. This has enhanced our understanding of fluid flow and reservoir characteristics (Wennberg and Rennan, 2018; Arif et al., 2021; Maniscalco et al., 2022; Liu et al., 2023). Cnudde and Boone (2013) showed that high-resolution μCT enables 4D

* Corresponding author.
E-mail address: ritwikchakraborty.96@gmail.com (R. Chakraborty).

monitoring of internal structural dynamics that aids in understanding stress- and time-dependant deformations of porous structures. Galindo et al. (2022) characterized synthetic carbonate rocks using μCT and petrography techniques to quantify pore spaces which provided valuable insights into fluid flow paths. Understanding the porosity and permeability of sedimentary rocks (e.g., sandstones, shales, limestones etc.) is useful, not only for estimating the potential yield of hydrocarbon reservoirs, but also for other applications such as geothermal energy (Kristensen et al., 2016; Cant et al., 2018), carbon sequestration (Saraf and Bera, 2021; Wang et al., 2023), and evaluation of diagenetic processes etc. (Zambrano et al., 2017, 2018). Sedimentary rocks often have partially to fully mineralized fractures over a wide range of scales (e.g., Laubach et al., 2019), and μCT has been used as a tool for fracture analysis in the past (e.g., Cappuccio et al., 2020; Yang et al., 2021).

In volcanic rocks, such as scoria and pumice, μCT investigations have been used to quantify the texture (Shape Preferred Orientation analysis) (Voltolini et al., 2011). It has also been used to understand the relation between microstructure and quality of building materials and restoration of archaeological sites/old structures (e.g., Cárdenes Van den Eynde et al., 2013; Punturo et al., 2023).

In metamorphic rocks μCT has been applied for textural analysis and 3D imaging of crystal and phase distributions (e.g., Denison et al., 1997; Cárdenes et al., 2016; Bhanot et al., 2017; Maurício et al., 2017; Corti et al., 2019; Bloise et al., 2020; Giamas et al., 2022). Often schists develop interesting microstructures viz. porphyroblasts, shear fabric, pressure shadows etc. (Passchier and Trouw, 2005). High-resolution X-ray computed tomography (HRXCT) has been effectively used for 3D imaging and detailed fabric analysis and textural quantification of porphyroblasts within schist samples (Ketcham, 2005; Aerden and Ruiz-Fuentes, 2020). Metamorphic rocks exhibit a wide range of mineral compositions, textures and stronger fabric alignment (compared to sedimentary rocks) as a result of recrystallization and deformation processes. This anisotropy can result in directional variations in rock strength, which can influence fluid flow and mineralization in metamorphic rocks (e.g., Vishnu et al., 2018). There are several examples of mineral deposits in metamorphic terrains – e.g., Uranium-Copper mineralization in Singhbhum Shear Zone (India; Pal et al., 2022), Gold-Tungsten deposit in Otago Schist (New Zealand; McKeag et al., 1989), Gold in Hutti Schist Belt (India; Radhakrishna and Curtis, 1999).

μCT is a technique that enables 3D visualization of rock microstructure as well as evaluation of its porosity/permeability. However, there is no major study till date that has focused on exploiting μCT data for measurement of petrophysical properties viz. porosity and permeability of metamorphic rocks. This research aims to fill this lacuna of exploiting μCT data for petrophysical characterization of metamorphic rocks and address the challenges associated with it. We have performed μCT analyses on mica schist samples from various depths taken from a borehole within the Singhbhum Shear Zone (Eastern India). We used the μCT data to analyse the porosity/permeability, as well as physically measure these properties for the same samples in the laboratory. This approach brings to light the challenges that geoscientists can encounter in extracting correct porosity/permeability of metamorphic rocks exclusively on the basis of μCT data. We demonstrate that laboratory measurements of porosity can be used as a basis to re-calibrate the greyscale threshold range of μCT data using a multiphase-field simulation framework. The "*Parallel Algorithms for Crystal Evolution in 3D*" (PACE3D) framework is an efficient and scalable phase-field solver (Hötzer et al., 2018), which in the past has been used in geosciences, for the study of crystal evolution, precipitation/dissolution and crack formation (e.g., Ankit et al., 2015; Prajapati et al., 2017, 2020; Späth et al., 2021, 2022a,b, 2023; Kumar et al., 2023; Späth and Nestler, 2023) and to match porosity/permeability simulations with lab measurements of porous sandstones (Monsees et al., 2020). In our present research, we have used PACE3D to perform threshold correction of greyscale digital CT values in order to obtain porosity equivalent to the laboratory measurement and follow this up with the analysis of anisotropy of porosity, permeability and hydraulic tortuosity of our schist samples.

By integrating laboratory measurements with phase-field modelling, our study significantly improves the reliability of μCT data and accuracy of petrophysical characterization of metamorphic rocks. The results of this integrated study are presented here and the implications of the findings in a natural geological example are discussed.

2. Geology of the study area

The brittle-ductile Singhbhum Shear Zone (SSZ) hosts several economically important mineral deposits of copper, apatite, magnetite and various radioactive minerals. The SSZ dates back to ca. 1.6 Ga. It stretches across a strike length of about 200 km and varies in width, reaching up to 4 km. The northerly dipping shear zone roughly delineates the boundary between the Archaean Singhbhum cratonic nucleus and the Proterozoic North Singhbhum Mobile Belt with top-to-south thrust movement of the northern hanging wall over the southern footwall (Mamtani et al., 2013). The Singhbhum Craton is characterized by a coalescence of ~3.45–3.29 Ga old Paleoarchean tonalite-trondhjemite-granodiorite-granite formations referred to as the Older Metamorphic Tonalite Gneisses and Singhbhum granitoid complex (Fig. 1). It also encompasses Paleoarchean to Mesoarchean greenstone belts, such as the Iron Ore Group comprising low-grade volcano-sedimentary rocks (Saha, 1994). High-grade supracrustal rocks, including ortho-amphibolites, para-amphibolites, pelitic schists, and quartzites belonging to the Older Metamorphic Group (OMG) are also present along with the late-stage (ca. 3.1 Ga) potassic granites (Mayurbhanj Granite). To the north of the cratonic nucleus lies the supracrustal province of the North Singhbhum Mobile Belt, which comprises the Chaibasa, Dhalbhum, Dalma, and Chandil Formations. The Chaibasa Formation in the hanging wall overlies the Dhanjori Group and consists of pelitic schists primarily composed of muscovite ± biotite ± quartz ± garnet (with retrogression of garnet to chlorite) which forms the predominant metamorphic mineral assemblage with occasional persistent layers of quartzite. The formation of the SSZ is characterized by lower greenschist facies P-T conditions. Various studies have emphasized the multi-phase deformation history of the SSZ which underwent a prolonged period of progressive deformation and is considered to have been reactivated at several time intervals (Ghosh and Sengupta, 1987).

Our study area lies within the SSZ. Borehole samples of schists belong to the immediate surroundings of Jaduguda, specifically within the marked study area in Fig. 1, reaching depths of ca. 1 km. To mitigate the influence of weathering, which is expected to be more significant in samples closer to the surface, our study exclusively focuses on borehole samples obtained from depths exceeding 100 m. Consequently, a total of five borehole samples were chosen accordingly from different depths (Fig. 2) for investigation at Indian Institute of Technology (IIT) Kharagpur, India. All the samples are schists with mostly chlorite, biotite, muscovite, quartz ± garnet (Chakraborty et al., 2022). As shown in Fig. 2, they have a strong foliation (schistosity) and show a layering that is identified by the variation in colour (light and dark layers in Fig. 2). This layering is on account of variation in mineralogical composition with the chlorite and mica (phyllosilicate) rich layers being darker. Some of the samples also show folded layering (e.g., sample from 598 m depth in Fig. 2) while some also have veins (e.g., sample from 1006 m depth in Fig. 2). Figure-3 illustrates the observed textures and microstructures in thin sections of schist samples from various depths. The grain size is variable in different samples and it is common for aggregates of quartz grains and phyllosilicates to be aligned parallel to one another, thus defining the schistosity in the mica schists (Fig. 3a–e). Garnet show porphyroblastic texture (Fig. 3a and b). In some schists quartz pressure shadows are present around garnet porphyroblasts (Fig. 3b). Quartz pressure shadows are also present around feldspar in a sample from 598 m depth. Microstructural studies reveal that the sample from 416 m depth has two distinct layers with contrasting grain size of

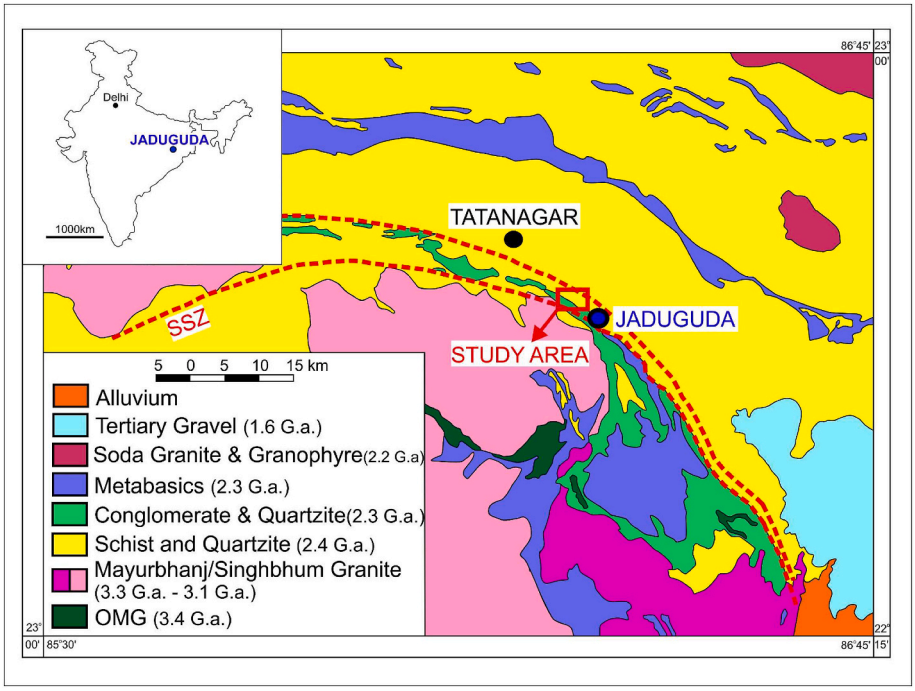

Figure-1. Regional geological map of the study area (after Saha, 1994). Samples investigated in this study are from the boxed area (marked by arrow) in the vicinity of the Singhbum Shear Zone (SSZ). T and J on the map refer to Tatanagar and Jaduguda, respectively. OMG in the index refers to the Older Metamorphic group of rocks.

quartz and phyllosilicates. These flaky mineral grains (mostly biotite, muscovite and chlorite) are abundant and closely spaced forming a heterogeneous compositional layering in these rocks. We consider that the parallel alignment of the various mineral phases may have an influence on the physical properties able to be evaluated using μCT.

3. Methods

The present study integrates several methods that are commonly used for measurement of petrophysical properties of rocks viz. X-ray micro-CT (μCT), and laboratory measurement of porosity and permeability. Additionally, microstructural simulation and multiphase-field modelling is performed to develop an enhanced understanding of the influence of heterogeneous layering on petrophysical properties. Details of the methods applied are presented in this section.

3.1. X-ray Micro-CT data acquisition, processing, and petrophysical property calculation

To investigate the petrophysical properties particularly porosity and permeability of the borehole schist samples, we have conducted non-destructive X-ray micro-CT (μCT) scans of samples from different depths (Fig. 2). μCT data were acquired from these five cylindrical core samples of ca. 7–8 cm length and ca. 3–4 cm diameter using a GE-phoenix model: V/TOME/XS machine by General Electric (GE) (present day manufactured by Waygate Technologies, Baker Hughes), housed in the Central Research Facility of IIT Kharagpur, India. The data acquisition process involved operating the machine at a voltage of 150 kV with a current ranging from 110 to 120 μA. Upon selecting the specified parameters, a detector calibration process is initiated to align and calibrate the detector. This calibration necessitates the temporary removal of the sample from the X-ray focal line. Following the calibration, the sample is automatically returned to its initially saved position and the scanning process starts. A μCT image is generated through the gradual rotation of the sample around a single axis of rotation while capturing a series of 2D radiographic images. The three-dimensional image can be reconstructed by applying reconstruction algorithms, such as the filtered back projection algorithm, and is subsequently saved as a volume file. For each of the five schist core samples investigated here, approximately 1500 two-dimensional image slices were generated during the scanning process in three different orientations viz. front, top and side (Fig. 4). These 2D grayscale image slices exhibit a voxel size, or the three-dimensional pixel size of ca. 45 to 50 μm. There is a trade-off between sample size and resolution as image resolution is often constrained by the required representative elementary volume (REV) for accurate porosity estimation and the geometric characteristics of the sample (Zhuang et al., 2022; Sadeghnejad et al., 2023). Consequently, the pore size of samples may fall below the image resolution. Determining an appropriate image resolution that effectively captures the true pore-scale properties poses a challenge, given that the chosen volume must adequately represent the characteristics of the entire porous medium. In this context, the entire borehole core samples were scanned to capture the heterogeneity and layering present within the cylindrical schist samples. For convenience of study the reference frame is chosen in such way that the long axis of the cylindrical core is chosen as z-direction while both the x- and y-directions represent the horizontal axes (Fig. 4).

Data acquisition was performed with the help of the Phoenix Datos/x CT software. Raw CT data were initially analysed using VGSTUDIO MAX 2.2 software at IIT Kharagpur (India), which involved filtering and corrections. Ring artefacts during data analysis were eliminated through Region of Interest (ROI) CT filtering, which maintained the material-to-background histogram ratio (Dinda et al., 2019). Beam Hardening Correction (BHC) filtering was used to reduce the artefacts introduced during the scanning process. Noise reduction was performed to enhance the clarity of the final images. Subsequently, the μCT data were processed to evaluate the petrophysical properties viz. porosity and permeability.

For porosity analysis, in the volumetric analysis section of the VGSTUDIO MAX 2.2 software (https://www.volumegraphics.com/en/products/vgsm.html), an automated thresholding algorithm of gray-scale values of the CT images was employed for void detection in every

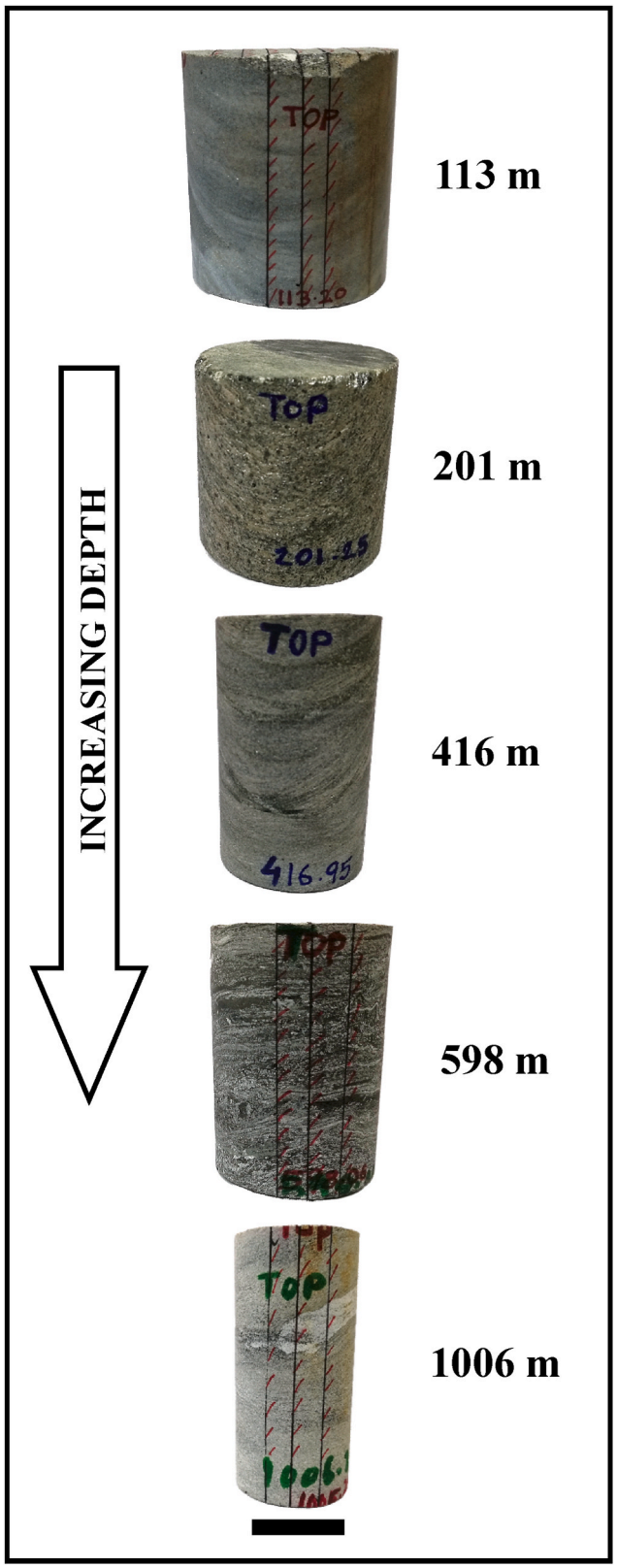

Figure-2. Overview of the 5 borehole samples (cores) investigated in the present study. The samples are arranged serially with increasing depth (mentioned beside each core); scale bar (black rectangle) is 3 cm. µCT imaging, as well as physical measurement of porosity and permeability of the samples was done in this study. See text for details.

sample. The black/dark regions represent pores, and can be easily distinguished and segmented from the solid matrix which is represented by white/brighter regions. Following the norm, values of 0 and 1 are respectively assigned to the pores/voids and the solid rock mass (e.g. Baveye et al., 2010; Huang et al., 2021; Zhao et al., 2023). As a representative example of the *modus operandi* adopted for porosity analysis using µCT data, Fig. 5 is presented. The latter is for a schist sample from the depth of 416 m, analysed using the software VGSTUDIO MAX 2.2. The 2D radiographic CT image slices exhibit pore spaces which are visualized with distinct colours in each of the three orientations viz. the top slice, the front slice and the side slice of the CT-scanned cylindrical core sample. The resulting 3D reconstructed volumetric image displays the pore network present within the sample. Pore spaces representing defects are differentiated by shades of blue and green corresponding to their respective void volumes (Fig. 5). For the analysis of permeability, the µCT data were processed using Avizo 9 Lite software (https://www.thermofisher.com/in/en/home/electron-microscopy/products/software/avizo-software.html) at the Indian Institute of Technology (IIT) Ropar, India with the same range of threshold values as used for porosity measurements.

Results of the porosity/permeability values of our schist samples calculated using the µCT data during initial processing are presented in section 4.1 (also see table, supplementary data-1). The latter establishes abnormally high values of porosity and permeability, when compared to those measured physically in the laboratory in similar metamorphosed schistose rocks (e.g., Bagde, 2000; Ganzhorn et al., 2019; Faulkner and Rutter, 2001; Dipple et al., 2005). This abnormality maybe due to (a) fine pore dimensions in metamorphic rocks (<0.1 µm; e.g., Zeng et al., 2022) that are difficult to resolve using µCT analysis and (b) challenges related to accurately identifying the threshold range while processing the CT data. This necessitates physical measurement of porosity and permeability in the laboratory on the same borehole samples for which µCT analysis was done.

3.2. *Laboratory measurement of porosity*

We carried out laboratory measurement of porosity in the schist samples using a gas pycnometer that is known to allow recognition of very fine pores (up to 3.5 nm diameter) and measure accurate porosity (Busch et al., 2017). Sample preparation for laboratory porosity measurements of the schist samples was performed using a drilling machine with water cooling at the Institute for Applied Geosciences - Structural Geology & Tectonics, Karlsruhe Institute of Technology (KIT), Karlsruhe, Germany. Plugs with a diameter of 2.5 cm were extracted from each large core sample. Preferably two cores were drilled out – one parallel (along the long axis of the cylinder referred to as the z-axis in Fig. 4) and the other perpendicular (along the horizontal x-axis) to the core axis of the cylindrical borehole samples; this was done to check for any directional-dependence of porosity. However, due to the smaller size of borehole samples from the depths of 201 m and 598 m, drilling could only be performed along the z-axis. As a result, porosity and permeability measurements for these smaller cores extracted from the relatively larger borehole samples from the above-mentioned depths were carried out in a single direction i.e., vertical axis or z-direction. The connected porosities of these smaller cores were determined using a micromeritics AccuPyc II 1340 pycnometer (Becker et al., 2019). Helium is introduced at less than 1.8 bar with a known cell volume. The device determines the solid volume as well as the density of the sample, excluding the void spaces present within the sample using Boyle's law. This solid volume can then be subtracted from the bulk cylinder volume (V), which can be calculated after determining the length (h), and radius (r) of the sample cylinders using formula $V = \pi r^2 h$. The difference is then divided by the bulk cylinder volume to determine the porosity percentage. The sensitivity of the instrument is 0.045 cm^3. Note that the samples were dried in a vacuum oven at 40 °C and 0.1 bar for at least 72 h prior to the porosity measurements.

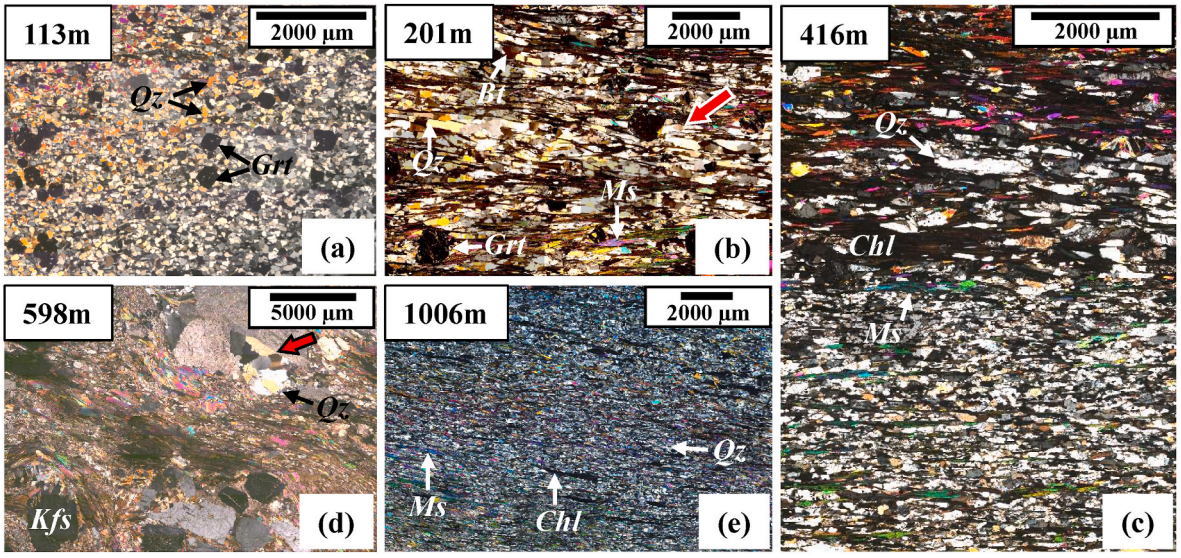

Figure-3. (a)–(e) are photomicrographs documenting representative textures and microstructures in thin sections of schist samples from different depths. The latter is mentioned at the top left corner in each photomicrograph. The grain size varies among different samples, with aggregates of quartz grains and phyllosilicates commonly aligned parallel to each other, defining the schistosity (a–e). Garnet displays a porphyroblastic texture in (a) and (b), while quartz pressure shadows around garnet porphyroblasts are shown by red arrow in (b). Quartz pressure shadows around feldspar are evident in the sample from 598 m depth which are indicated by red arrow in (d). The sample from 416 m depth in (c) exhibits two distinct layers with contrasting grain sizes of quartz and phyllosilicates. Flaky mineral grains, mainly biotite, muscovite, and chlorite, are abundant and closely spaced, forming heterogeneous compositional layering. Mineral symbols for each mineral phases are mentioned in each photomicrograph. (Mineral abbreviations: Quartz: Qz, Garnet: Grt, Biotite: Bt, Muscovite: Ms, Chlorite: Chl, K-feldspar: Kfs). (For interpretation of the references to colour in this figure legend, the reader is referred to the Web version of this article.)

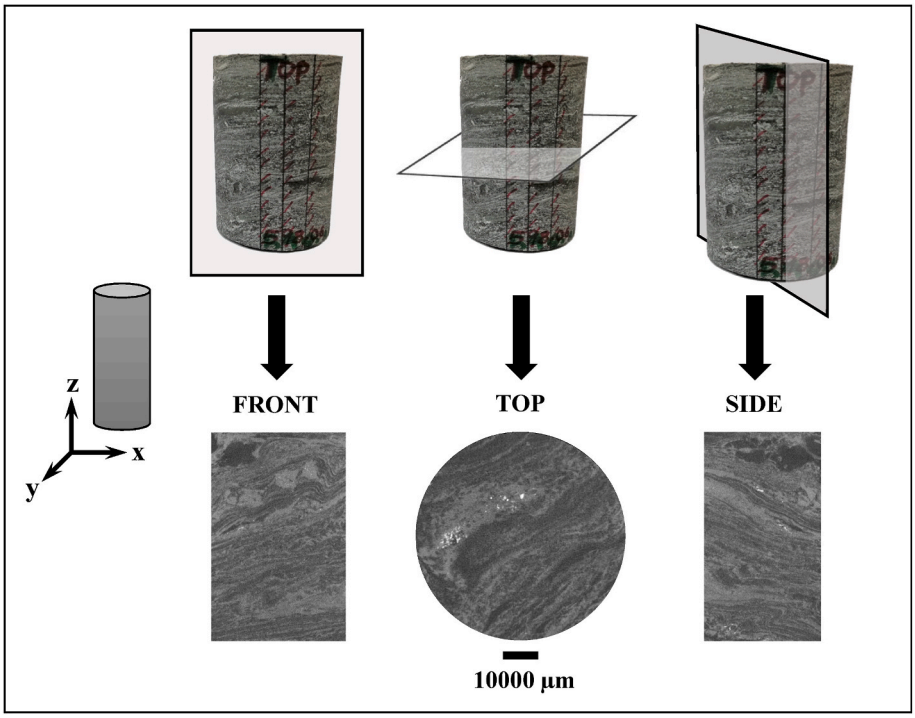

Figure-4. Front view, top view and side view of a schist core (sample from 598 m depth) obtained after µCT scanning. Note that for reference the long axis of the cylinder is considered "z", whereas "x" and "y" axes are horizontal. See text for details.

3.3. Laboratory measurement of permeability

The permeability of the sample cylinders was measured using a steady-state air permeameter manufactured by Westphal Mechanik (Germany), housed in the Institute for Applied Geosciences - Structural Geology & Tectonics, KIT Karlsruhe, Germany. The core sample was placed in a silicon sleeve to apply a confining stress of 1.2 MPa to avoid sample bypass. Using dry, oil-free, lab air (80% N_2, 20% O_2) an upstream pressure between 0 and 0.6 MPa can be adjusted to facilitate gas flow through the sample. At the upper end of the measuring cylinder, the flow rate of the gas is measured, which depends on the permeability of the rock. The permeability of the sample can be calculated using Darcy's law

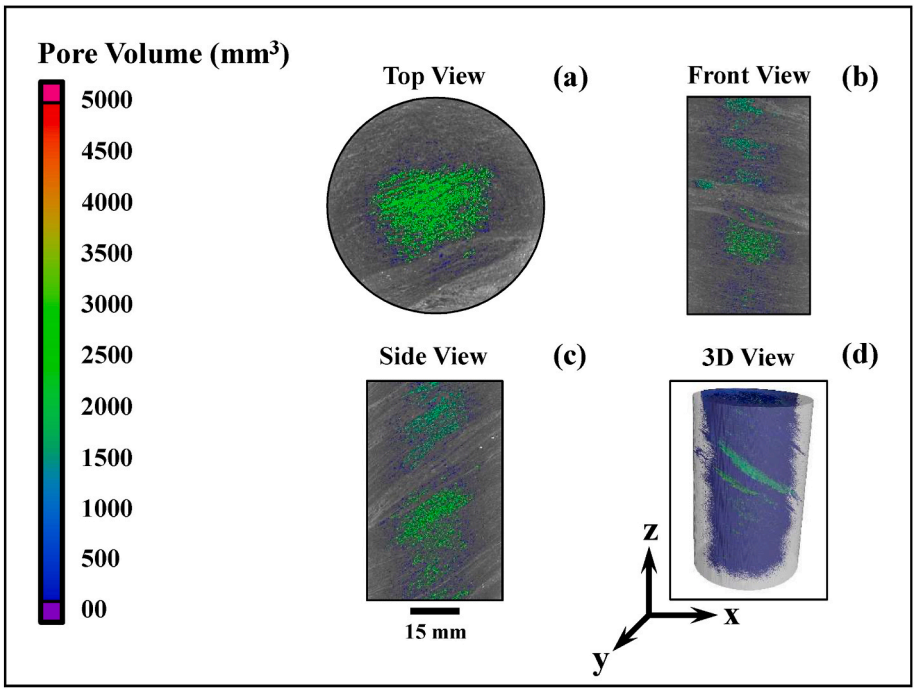

Figure-5. Porosity determination from μCT data of a schist sample (416 m depth) using the commercial software VGSTUDIO MAX 2.2. (a), (b) and (c) are respectively the top, front and side view of one of the image slices in each of these orientations. The 3D representation of the pore network is presented in (d), where the pore spaces (defects) are indexed in blue and green colours according to their volume. (For interpretation of the references to colour in this figure legend, the reader is referred to the Web version of this article.)

(eq. (1)):

$$K = Q l \eta / A \Delta p \quad (1)$$

where, K = Permeability in m^2, Q = Flow rate in m^3/s, determined by the instrument, η = Dynamic viscosity of the permeant in $N.s/m^2$, a function of the ambient temperature, l = Length of the sample body in meters, determined by vernier callipers, A = Cross-sectional area of the sample body in m^2, Δp = Pressure difference in N/m^2, determined by the instrument. The measured permeability is then converted into Klinkenberg-corrected permeability (Klinkenberg, 1941). The conversion is performed using equation (2):

$$K_a = K_L \Big/ \left\{ \frac{1 + 0.5 K_L^{-0.37}}{P_m} \right\} \quad (2)$$

Where, K_a = Apparent permeability, K_L = Klinkenberg permeability and P_m = Mean pressure. The air permeameter has a measurement range of 0.001–10,000 mD. Measurements below the measurement limit are displayed as 0.0001 mD. All the measurements were conducted under laminar-flow conditions at ambient laboratory temperature (T = 22 °C) and until steady-state flow conditions were achieved (Monsees et al., 2021).

3.4. *Phase-field simulation of porosity and permeability using μCT data*

The phase-field method uses a mathematical model for describing interfaces (e.g., grain boundaries) in a diffuse way and therefore avoids the need for complex interface tracking or remeshing algorithms (Steinbach et al., 1996). In this work, the phase-field method was used for modelling the porosity/permeability in the schist samples (cylindrical cores) at the macroscopic and microscopic scales. We used the multi-physics phase-field solver PACE3D (https://www.h-ka.de/idm/profil/pace3d-software#c17807), in which the multiphase-field equations are implemented (see Hötzer et al., 2018 for details of the implementation and a description of optimization algorithms). PACE3D is used to compute the permeability of the cylindrical schist samples in horizontal and vertical directions. The Darcy equation is solved in each spatial point, whereas a permeability tensor is given as an input value for each material phase (e.g., phyllosilicates, pores). An isotropic permeability tensor is used

$$\mathbf{k}^{\alpha} = \begin{pmatrix} k_{iso}^{\alpha} & 0 & 0 \\ 0 & k_{iso}^{\alpha} & 0 \\ 0 & 0 & k_{iso}^{\alpha} \end{pmatrix}$$

for the two or three occurring phases α. This work incorporates both the modelling of the entire core at the cm-m scale and the resolution of the granular structure at the microscale.

3.4.1. *Modelling fluid flow on macroscale*

In the work-flow, μCT data were employed to numerically simulate fluid flow in the cores. As a preliminary step, the acquired μCT data were segmented. The DICOM data files were imported into a pre-processing Python method to read the data. Subsequently, the greyscale values were classified into either two phases (pore and rock mass) or three phases (pore, other mineral phases and phyllosilicates), which were present in the quartz mica schists. The two-phase segmentation was chosen as a first step to validate if the simulations generally agree with the laboratory measured permeabilities. The complexity of the approach was subsequently increased and an additional phyllosilicate phase was segmented from the μCT data.

For the segmentation of porosity, the lower and upper threshold values were calibrated accordingly to match the porosity measured in the laboratory experiments described in section 3.2 (refer to results in section 4.2). The remaining material volume was assigned as rock-phase in the two-phase model (see supplementary data-2). In the three-phase model, the threshold values for the phyllosilicate-rich layers were set such that the volume percentage of the phyllosilicates in total was ca. 50% of the entire CT scanned core volume. This aligns with the characteristics of the natural mica schist samples, and the observable

phyllosilicate layers in the hand specimens correspond with the layering as seen in the μCT data. The remaining regions were set to rock-phase, and the segmented data were exported into PACE3D data format (see section 4.3.2). Subsequently, fluid dynamics simulations were conducted.

3.4.2. Modelling fluid flow on microscale

Due to the presence of a prominent interface between phyllosilicate-rich layer and quartz-rich layer in the strongly foliated 416 m depth sample (Fig. 3c), it is suspected that there may be additional effects of strain variation/partitioning on the microscale which affect the permeability. The authors hypothesize that the grain boundaries are not as strong as in other core samples and this might be responsible for increasing the permeability along the grain boundaries. Therefore, the permeability is decreased along the diffuse interface with the following equation (3):

$$k_{eff.} = k_{iso} \quad 4\phi_1\phi_2\left(\phi_1 k_1 + \phi_2 k_2 \quad k_{gb}\right) \tag{3}$$

Where $k_{eff.}$ represents the effective/resulting permeability at a spatial point, k_{iso} is the isotropic permeability of the rock structure, ϕ_α and k_α denote the volume fraction and (isotropic) permeability of phase α, and k_{gb} is the prescribed permeability at the grain boundary. The results of this approach are presented in section 4.3.3, where the numerical polycrystalline microstructure that mimics the natural rock is used for analysis in PACE3D.

Additionally, the effective permeability is decreased in distinct directions to include the effect of structural anisotropy (e.g., highly strained grains in x-direction). The resulting permeability tensor for the Darcy equation is then given by

$$k = \begin{pmatrix} \xi_x k_{eff.} & 0 & 0 \\ 0 & \xi_y k_{eff.} & 0 \\ 0 & 0 & \xi_z k_{eff.} \end{pmatrix}$$

Where the permeability in x, y, and z-directions can be modified by ξ_x, ξ_y and ξ_z (ξ is the constant factor in x, y and z directions used to scale the effective permeability for better simulation analysis). As an example, the resulting permeability is plotted with this new approach (section 4.3.3).

As stated earlier, a layered anisotropic structure with elongated grains was developed for carrying out the microstructure simulations. In order to assess the permeability of this microstructure, a pressure gradient was applied both perpendicular and parallel to the layers (refer to results in section 4.3.3).

4. Results

The schists, whose petrophysical property measurements are the focus of the present investigation, are strongly foliated and also have a compositional variation (as mentioned in section 2). Although all the rocks are schists, the grain size and layering in rocks from different depths is not identical. Some samples show a strong schistosity (Fig. 3e), while others are less foliated (Fig. 3a). Some schists show quartz pressure shadows around coarse grains of garnet (Fig. 3b) and feldspar (Fig. 3d). In addition, some of the schists also have a layering defined by phyllosilicates and quartz grains of different size (Fig. 3c). The 3D microstructure of each schist sample (core) was imaged using μCT following the method explained in section 3.1. Supplementary data-3 documents the microstructure recorded from μCT in all the investigated cores (samples). Accordingly, samples from all the depths show a layered microstructure. Schists from 201 m depth to 1006 m depth typically exhibit a strong planar fabric due to the alignment of phyllosilicates (viz. muscovite and biotite), which is reflected in the 2D radiographic CT images (supplementary data-3). The sample from 201 m depth is replete with garnet porphyroblasts. Since garnet is denser than the matrix mineral phases (mica and quartz), the garnets appear as bright spots in the radiographic image of this sample. Whilst folds can be seen in the hand specimen of 598 m depth sample, the μCT images help in visualising the continuity of the structure inside the core. Similarly, the continuity of the vein in sample from 1006 m depth is recorded in the μCT radiographs. It maybe noted that the vein is of quartz, which is a lower density phase from the matrix minerals of the schist, thus appearing dark grey in the radiographs. Importantly, the pores (including fractures) appear black (darkest) in the radiographs. Some of these black areas (pores/fractures), which are visible at the scale of the figure in an individual slice of an image stack of μCT data are marked by arrows in supplementary data-3. The variation in the distribution of these pores can be visualized qualitatively with the study of image stacks of a core in μCT data files (using any μCT visualization software). Since the distribution of pores in samples from different depths is not uniform, it is envisaged that the porosity (as well as connected porosity/permeability) will be variable. Further, since these rocks have a fabric anisotropy (see Chakraborty et al., 2022), they may have anisotropic distribution of their petrophysical properties. In this section, we present detailed results of porosity and permeability calculations obtained by utilizing various techniques like μCT, laboratory measurements, computationally determined porosity and permeability through multiphase-field simulations, and findings from numerical microstructure simulations.

4.1. Porosity and permeability from μCT data – initial processing

Porosity was determined to be in the range of approximately 2%–6% as analysed from the μCT data of the five borehole schist samples calculated using the software VGSTUDIO MAX 2.2. Permeability values in the order of 10^5 Darcies (Fig. 6) were calculated with Avizo 9 Lite software using the same threshold range as used for the porosity calculation. It may be noted that these measurements were made for directions along the long axis (z-axis) of the cylindrical cores. The obtained porosity percentages were then plotted against depth. Higher porosity values of 5.98% and 5.1% (±0.491%) are observed in the schists at the depths of 416 m and 598 m, respectively (Fig. 6a) while the shallower depths of 113 m and 201 m exhibit relatively low porosity values of 2.87%–3.74% (±0.557%) respectively. The deepest sample from 1006 m yields a porosity value of 3.88% (±0.05%).

The permeability values are also plotted against depth (Fig. 6b). The permeability values of the schists from shallower depths are 2.95×10^4 D and 1.69×10^4 D (samples from 113 m and 201 m depth, respectively) with an error range of $2.32 \pm 0.686 \times 10^4$ D. A peak value of 157.59×10^4 D was observed at the depth of 598 m followed by 134.49×10^4 D at 1006 m depth (with an error range of $146 \pm 12 \times 10^4$ D). These permeability values determined from μCT data are overestimated and are several orders of magnitude greater than what is expected for mica schists, which usually have permeabilities in the range of 10^{-2} mD to 10^{-6} mD (Faulkner and Rutter, 2001; Dipple et al., 2005). The notable disparity in values may be due to the usage of automated thresholding of the grayscale values in the digital CT images by the authors. This necessitated laboratory measurement of porosity and permeability of the schist samples (section 3.2, 3.3) and the results are presented in section 4.2.

4.2. Porosity and permeability from laboratory measurements

Laboratory porosity and permeability (Klinkenberg-corrected) data from the five borehole schist samples from different depths are presented in table-1. A total of eight small cores (five cores along the z-direction and three cores along the x-direction as represented in Fig. 4) were extracted from the large borehole core samples. The direction along which the core was drilled from the large cylindrical sample is mentioned in suffix of the sample numbers representing different depths. The porosity percentages along the perpendicular or z-axis varies between 1.3%–4.5%, while it falls within the range of 0.7%–2% along the horizontal or x-axis. Klinkenberg-corrected laboratory

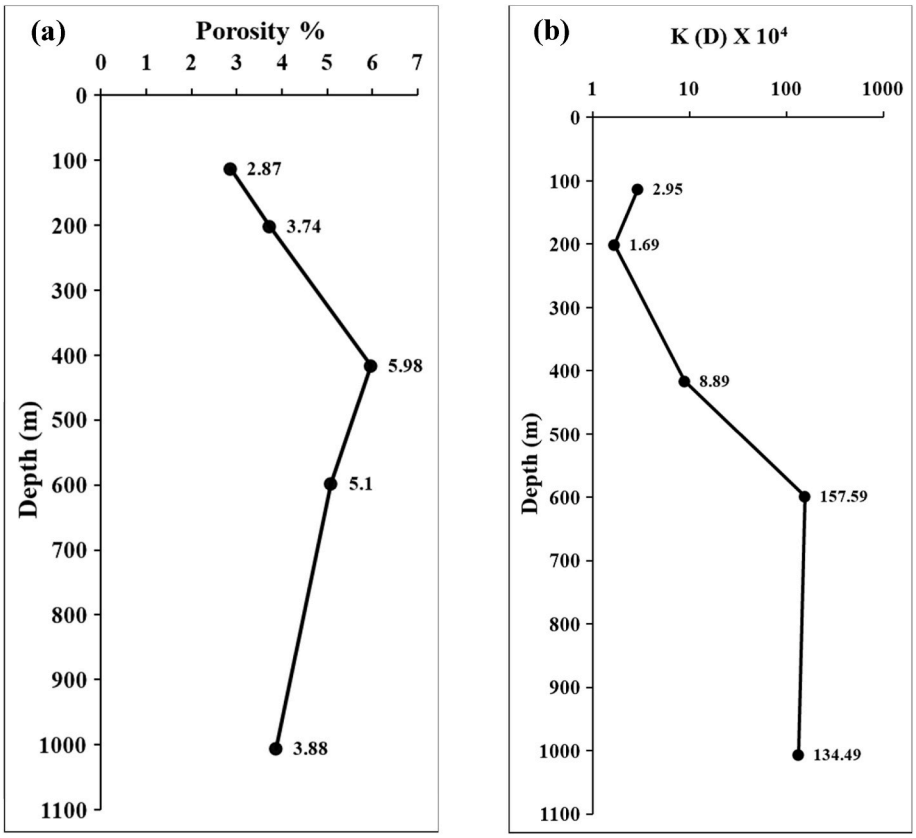

Figure-6. (a) Depth vs. porosity graph of the schist samples. (b) Depth vs. permeability (K) graph of the schist samples. The porosity and permeability are based on processing of μCT data using commercial software, VGSTUDIO MAX 2.2 and Avizo 9 Lite, respectively. Note that the values are abnormally high as compared to those known from similar metamorphic rocks. See text for details.

Table-1
Laboratory (Lab) porosity and Lab-permeability data for the schist samples from different depths. Lab-Porosity was measured using AccuPyc II 1340 pycnometer, while the Lab-permeability was measured with an air permeameter by Westphal Mechanik (Germany); data were acquired at Karlsruhe Institute of Technology (Germany). The measurements were made in small cores extracted from the large cylindrical borehole samples along both the z- and x-directions (long and horizontal axes respectively as illustrated in Fig. 4), which is indicated by the suffix of sample numbers. Lab-permeability values are Klinkenberg-corrected measured in millidarcy (mD).

Sample No.	L (mm)	d (mm)	Lab-Porosity (%)	Lab-Permeability(Klinkenberg-corrected; mD)
113-z	26.00	25.30	2.68278585	0.000100
201-z	12.60	24.80	1.8755167	0.001507
416-z	11.60	25.30	3.75051999	0.000100
598-z	21.95	24.85	1.30448745	0.000348
1006-z	5.95	25.30	4.50374535	0.000100
113-x	25.95	24.80	2.03811086	0.000100
416-x	24.10	24.70	0.73210154	0.530151
1006-x	13.35	24.85	1.1052735	0.001135

permeability values lie within the range of 0.0001 mD – 0.0015 mD along the z-axis, whereas it varies between 0.0001 mD – 0.5 mD along the x-axis. Fig. 7a is the depth vs. laboratory porosity plot. This reveals the porosity changes with increasing depth in the schist samples and also the directional variations in individual samples. Similarly, depth vs. laboratory Klinkenberg-corrected permeability plot (Fig. 7b) shows that the permeability is higher along the horizontal (x-direction) than the permeability along the z-direction for the samples at 416 m and 1006 m depths. The permeability also varies with increasing depth. To evaluate directional anisotropies, it is essential to determine the β-angle, which represents the angle between the foliation plane and the core axis of the cylindrical borehole core sample. Histograms in Fig. 8 depict the relationship between β-angle and laboratory porosity and laboratory Klinkenberg-corrected permeability obtained along both the z and x-directions for the schist samples from different depths (except for the samples from 201 m to 598 m depths). It is observed that with a β-angle of 50°, the sample at 416 m depth shows higher porosity along the z-axis (Fig. 8a) and high permeability along the x-axis (Fig. 8b). A similar trend is shown by the samples at 113 m and 1006 m depths with β-angles of 65° and 77°, respectively (see Fig. 8).

4.3. Computationally determined porosity and permeability using multiphase-field simulations

4.3.1. Results from 2-phase simulations

The simulated-porosity (see Table 2) determined from the segmentation of the μCT data of the large borehole samples from different depths were calibrated accordingly to align with the laboratory measured porosity values mentioned in section 4.2. For comparison, the laboratory (lab) porosity in smaller cores extracted from the large samples in x and z orientations is also plotted in the same depth vs. porosity graph along with the simulated-porosity (Fig. 9). However, the simulated-porosity did not show any directional variations.

For the two-phase simulations, the permeability was set as $k_{iso}^{rock} = 0.0001$ mD and $k_{iso}^{pore} = 10$ mD. The value for the rock-phase (consisting of quartz and feldspar) was chosen such that it corresponds to the permeability of natural granites which ranges around 10^{-3} to 10^{-4} mD (Kranz et al., 1979) and the pore-phase permeability was chosen multiple orders higher than the rock-phase since the permeability is higher in the void regions.

The fluid flow simulations were performed in horizontal and vertical

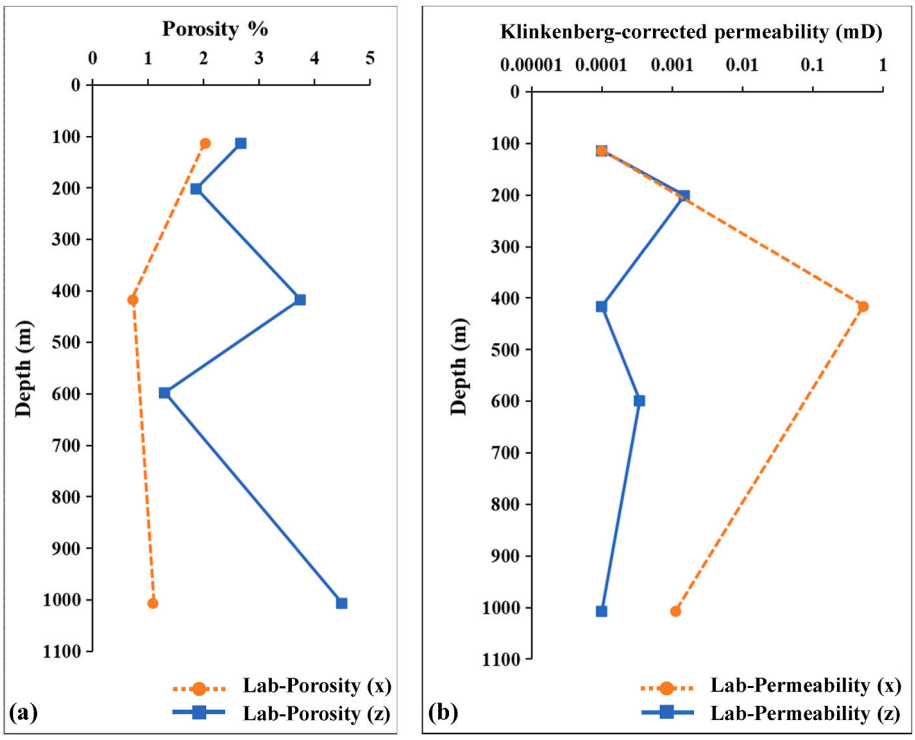

Figure-7. (a) Depth vs. laboratory (Lab) porosity graph and (b) Depth vs. laboratory Klinkenberg-corrected permeability graph of the schist samples. As indicated in table-1, the porosity and permeability measurements were made in small cores extracted from large borehole samples along z and x-directions. The obtained results in the two directions are plotted here.

direction of the segmented cores (refer to supplementary data-2) and the measured permeability in each direction (x, y and z) (Table 2) for all core samples is plotted in Fig. 10, together with the laboratory measured permeabilities. The simulations show a good agreement with the laboratory values at 113 m and 1006 m depth, however they show an underestimation of the measured permeability at 201 m and 598 m depth and a large deviation from the laboratory measurements at 416 m depth.

Additionally, the hydraulic tortuosity ($\tau_h = |\mathbf{u}|/u_{stream}$, where τ_h is the hydraulic tortuosity, $|\mathbf{u}|$ is the mean value of velocity throughout porous medium and u_{stream} is the component of fluid velocity along the flow direction) of the fluid flow was analysed to determine the anisotropy of the flow paths in vertical and horizontal directions (Fig. 11). The flow paths for the 201 m and 416 m samples are found to be more anisotropic than the paths in the 113 m, 598 m and 1006 m sample. However, in each direction of the corresponding cases they are nearly the same.

4.3.2. *Results from 3-phase simulations*

For the three-phase simulations of the segmented cores (Fig. 12), the same permeability values were used as in the two-phase simulations for rock- and pore-phases. For the phyllosilicate-phase, $k_{iso}^{phyllosilicate} = 0.00015$ mD was chosen. The above value for the phyllosilicates was chosen since the permeability along the phyllosilicate-rich layers which defines the foliation in the mica schists is expected to be higher than the remaining rock volume (consisting of quartz, feldspar ± garnet) (Leclere et al., 2012).

The resulting permeability computed from the simulations (see Table 2) in comparison with the laboratory measurements along different directions (parallel and vertical to the drilling direction) are depicted in Fig. 13. The simulated permeabilities for both the directions show a good agreement with the laboratory measurements for all samples except the 416 m depth sample. The computed permeabilities lie here in between the laboratory data as evident in the permeability vs. depth graph (Fig. 13). Due to the disparity in sample sizes between the numerical and laboratory samples, it is hypothesized that heterogeneity in the 416 m depth sample may be responsible for this difference. Therefore, smaller sized cutouts (same volume as used in the laboratory measurements) were extracted from the numerically modelled rock and their permeability was analysed. The two points plotted as box and circle with a cross in Fig. 13 showcase the lowest and highest measured permeability of the cropped regions from z- and x-directions, respectively. Even though they lie closer to the laboratory measured values, a deviation is still possible. Moreover, the hydraulic tortuosity computed for this three-phase model (Fig. 14) show a similar trend as that of the two-phase model.

4.3.3. *Results from microstructure simulations*

For the existing disparity between simulated and laboratory values even in the three-phase system, the macroscopic simulations were extended to microscales suspecting that additional factors are influencing the resulting permeability in the more heterogeneous 416 m sample. In the microstructure simulations, the authors set $\xi_x = 10$ (horizontal direction; highly strained grains) and $\xi_y = 1$ (vertical direction), $k_{gb} = 1$ mD, and $k_{iso} = 0.0001$ mD for all grains and used the numerical microstructure depicted in Fig. 15b. After applying a pressure gradient perpendicular and parallel to the layering, the flow anisotropy was analysed by measuring the resulting permeability. In comparison to the laboratory measured data, a similar trend was achieved with this modelling approach (Fig. 15e and f). As anticipated, when the flow parallels with the layering, the resulting permeability is significantly higher compared to the flow perpendicular to the layering. The measured permeability in the simulations closely matches the permeability recorded in the lab experiments (Fig. 15f).

5. Discussion

Our research has brought out interesting insights into utilizing X-ray micro-CT (μCT) for the petrophysical analysis of metamorphic rocks.

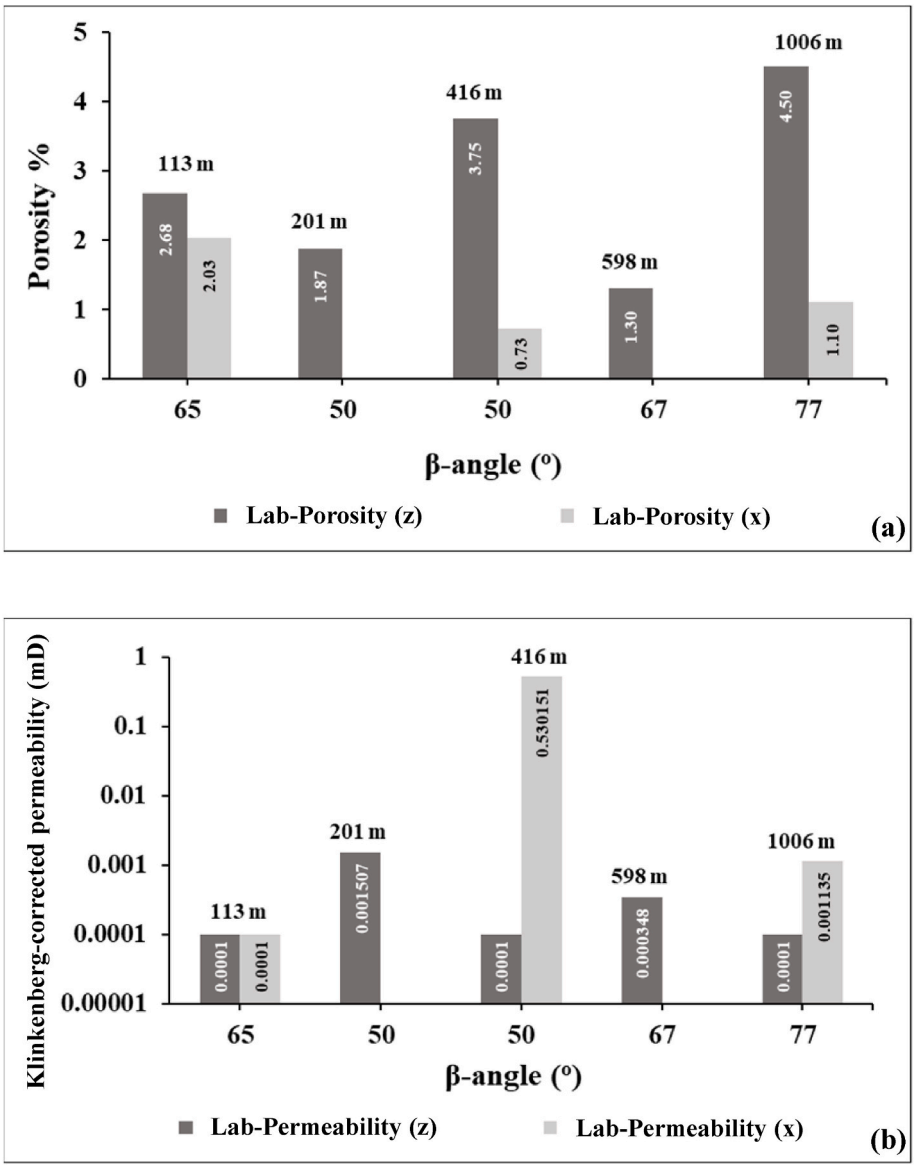

Figure-8. Histograms depicting the relationship between β-angle vs. laboratory (Lab) porosity (a) and β-angle vs. laboratory Klinkenberg-corrected permeability (b) for the schist samples from different depths. The dark grey histogram represents values along z-direction and the light grey histogram represents values along x-direction. The Lab-porosity and Lab-permeability values are mentioned within each histogram, and the depth (m) is also indicated.

Table-2

Three-dimensional simulated porosity, permeability and hydraulic tortuosity data of the schist samples investigated in this study. The simulations were done by applying PACE3D framework to μCT data described earlier in three perpendicular directions (x, y and z; see Fig. 4). Permeability and hydraulic tortuosity simulations yield different values in the three directions, while porosity is constant in all directions. The simulations were done considering 2-phases (rock volume that includes all mineral phases and pore volume) and 3-phases (phyllosilicates, pore volume, and other mineral phases).

Depth (m)	Simulated Porosity (%)	2-phase Simulated Permeability (mD)			3-phase Simulated Permeability (mD)			2-phase Simulated Hydraulic Tortuosity			3-phase Simulated Hydraulic Tortuosity		
		x	y	z	x	y	z	x	y	z	x	y	z
113	2.520048	1.62E-04	1.63E-04	1.61E-04	1.76E-04	1.77E-04	1.74E-04	1.20398	1.20494	1.19924	1.29773	1.29956	1.28578
201	1.825057	2.36E-04	2.78E-04	2.36E-04	1.99E-03	3.30E-03	7.90E-04	1.55546	1.48788	1.46704	1.98967	1.70624	1.96708
416	3.723669	4.04E-04	3.85E-04	3.31E-04	1.18E-02	1.04E-02	4.38E-03	1.52549	1.53794	1.51443	1.78143	1.78143	1.92184
598	1.308247	1.64E-04	1.69E-04	1.37E-04	3.41E-04	3.50E-04	2.33E-04	1.26654	1.28246	1.19078	1.67296	1.69481	1.50519
1006	1.110944	1.19E-04	1.19E-04	1.18E-04	1.92E-04	1.94E-04	1.84E-04	1.06968	1.07041	1.06532	1.2471	1.25	1.22005

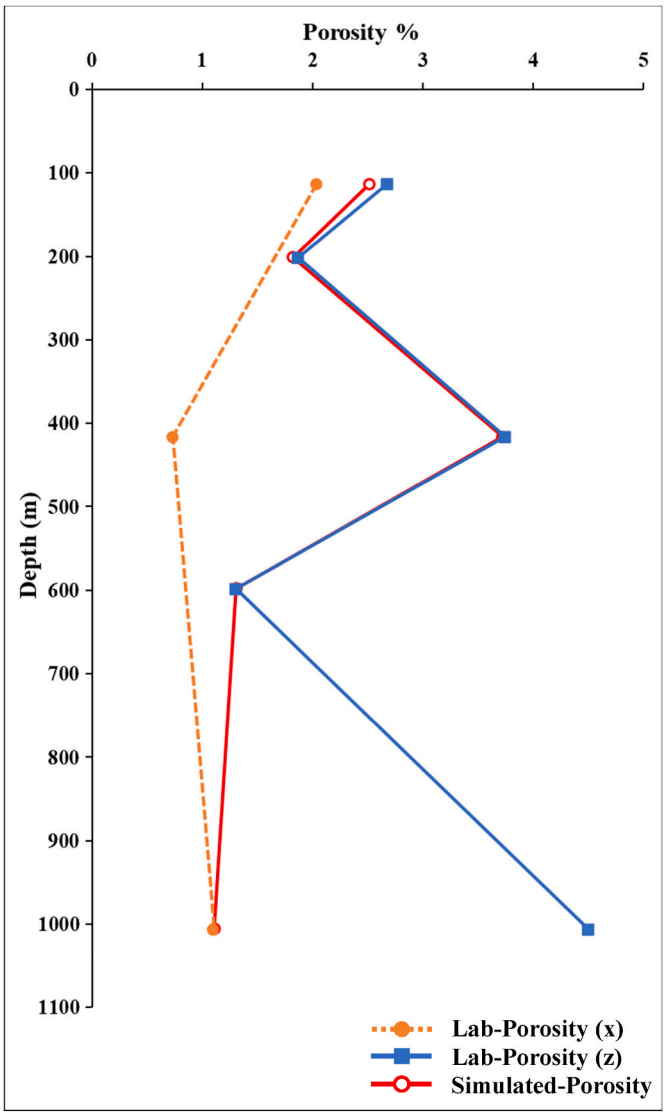

Figure-9. Depth vs. porosity graphs of the investigated schist samples. The simulated-porosity determined from μCT data of the large borehole samples from different depths is plotted. The simulated-porosity was calculated using PACE3D framework (IAM-MMS, KIT Karlsruhe, Germany). For comparison, the laboratory (Lab) porosity in smaller cores extracted from the large samples in x and z orientations is also plotted in the same diagram.

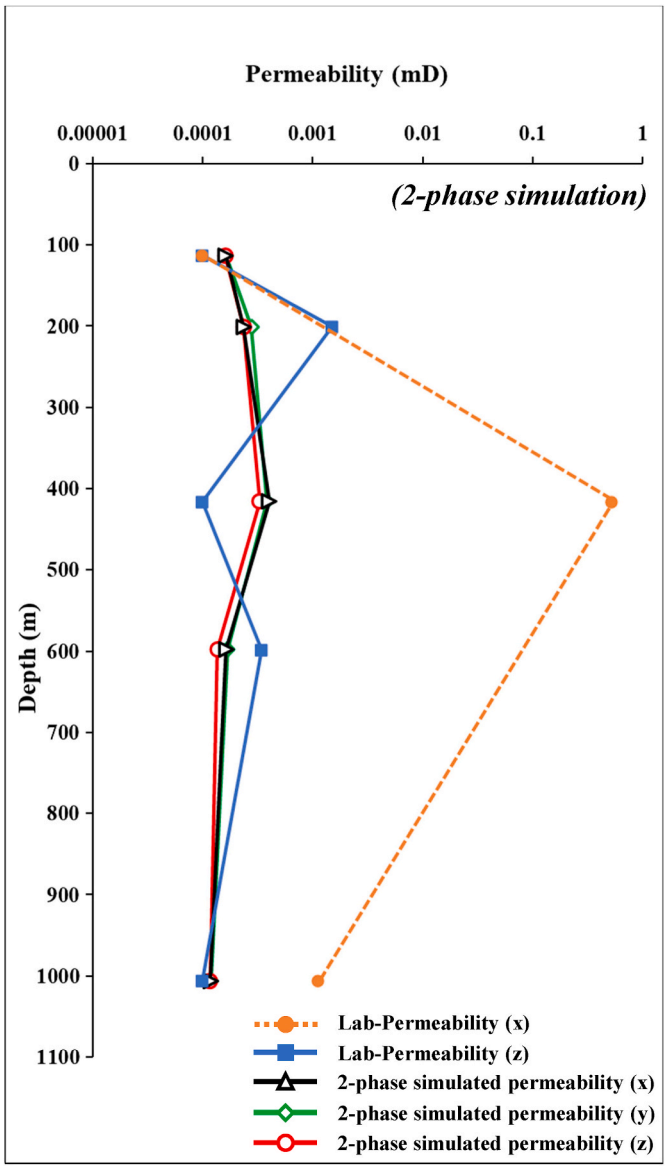

Figure-10. Depth vs. permeability graphs of the investigated schist samples. The laboratory (Lab) permeability in cores from two directions (x and z; see Fig. 4) are plotted. The three dimensional 2-phase simulated permeability (PACE3D framework applied to μCT data) determined in x, y and z directions is also plotted. Note that there is a significant difference in the Lab-permeability and 2-phase simulated permeability for the sample from 416 m depth. See text for details.

The present study has shown that μCT data processing algorithms in commercial software are unable to perform accurate thresholding of greyscale values to index voids in schists without calibrating with laboratory derived porosity values, thus leading to an overestimation of their porosity. This is due to the compact structure and very fine pores that cannot be well-resolved with μCT analysis. A similar challenge is also faced with porosity quantification of shale using μCT. In case of shale, one of the methods by which this problem has been resolved is by performing μCT studies of Helium-injected shale samples along with several other contrasting agents. This enhances the pore resolution under μCT, thus helping in more reliable porosity determination (Fogden et al., 2014; Mayo et al., 2015). Some researchers have also used multi-scale imaging techniques (such as Neutron Tomography, Focused Ion Beam-SEM and SEM imaging) to calculate porosity of shale samples (Ramos et al., 2019; Garum et al., 2020; Arif et al., 2021).

In contrast to the above approaches for shale, in the case of schists investigated by us, we have used a combination of laboratory measurement of porosity of the samples, μCT data and microstructural simulation to quantify porosity and further study its anisotropy as well as other petrophysical properties. We measured the porosity of an individual schist sample with a gas pycnometer. Subsequently, we performed threshold correction of greyscale digital CT values of an individual sample to obtain the porosity equivalent to the laboratory value of that sample; this was done using PACE3D. Finally, this corrected threshold was applied to calculate permeability and tortuosity. The details are discussed in the present section. It may be noted that, although the data discussed here pertains to mica schists, similar implications can be expected for other metamorphic rock types as well.

5.1. Importance of laboratory measurements in fixing the threshold for automated porosity and permeability calculations of the μCT data

The porosity and permeability values computed from μCT data are

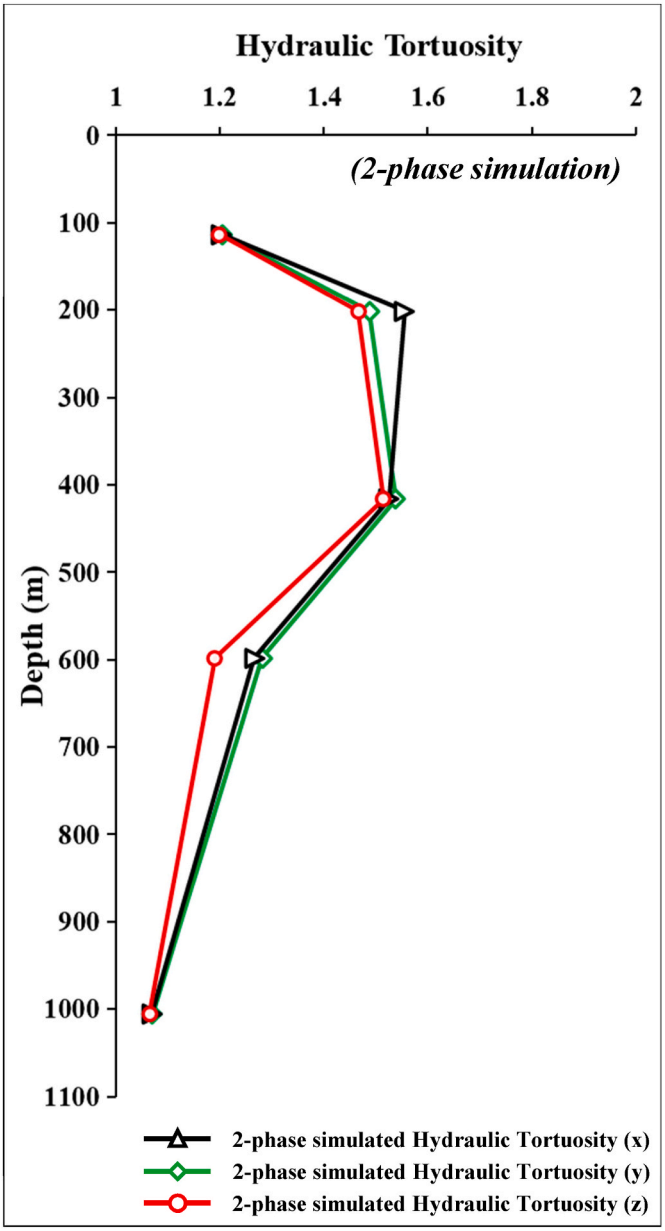

Figure-11. Depth vs. 2-phase simulated hydraulic tortuosity plots for the schist samples. The tortuosity was simulated by applying PACE3D framework to μCT data in three directions (x, y and z). See text for details.

higher (5%–6% for porosity and 10^5 D for permeability) than those obtained by physical measurements in earlier studies (Bagde, 2000; Faulkner and Rutter, 2001; Dipple et al., 2005; Ganzhorn et al., 2019) (Fig. 6). According to us, these high values are a consequence of the automated thresholding of grayscale values of the CT images by the software used for analysis (VGSTUDIO MAX 2.2 and Avizo 9 Lite). Metamorphic rocks are known for their complex and heterogeneous nature. Fixing the threshold for porosity and permeability calculations of μCT data for impermeable metamorphic rocks can be a challenging task. They are deformed and exhibit a wide range of mineralogical compositions, grain sizes and textures making it difficult to identify a consistent threshold that accurately differentiates between the solid volume and pore spaces. These rocks have very low porosity, with pores that are extremely small and scattered. The choice of threshold can be highly sensitive to these small variations, and a minor adjustment in the threshold value can significantly impact the calculated porosity and permeability.

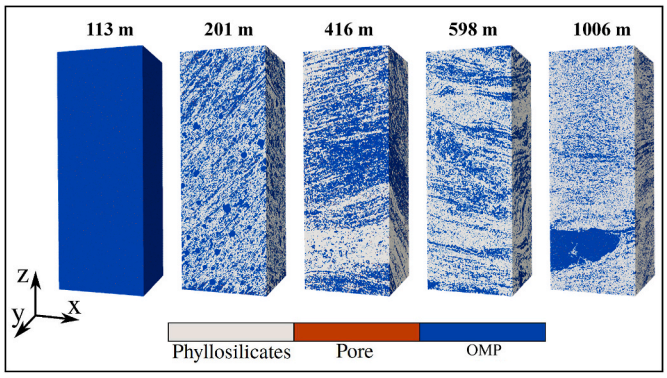

Figure-12. Three-dimensional visualization of the 5 schist samples based on simulation of X-ray μCT data using the PACE3D framework. The simulation considers each rock to comprise 3 phases viz. phyllosilicates (grey), pores (red) and other mineral phases (OMP; blue). Note that the x, y and z directions in the simulations are kept the same as in Fig. 4. (For interpretation of the references to colour in this figure legend, the reader is referred to the Web version of this article.)

To address the challenge posed by these high and unrealistic values, an alternative approach was implemented. Our study establishes that to logically analyse μCT data for porosity and permeability calculations, laboratory measurements play a pivotal role in setting the threshold for automated calculations. Porosity and permeability influence the rock material characteristics and are intricately linked to the grayscale intensity values within the μCT scans. A threshold range set too high or too low can skew the results, affecting the accuracy and reliability of the analysis. Hence, determining an optimal threshold to differentiate between rock volume and void spaces is crucial in accurately characterizing these parameters. The significance of laboratory measurements lies in calibrating these thresholds against physical observations or direct measurements. Laboratory measurements yielded more plausible values, with porosity ranging from 1% to 2% and permeability in the range of 10^{-3} to 10^{-4} mD (Fig. 7). By using the laboratory obtained porosity and permeability values as a reference, it became possible to calibrate the threshold used by the automated algorithms required for μCT analysis; this addresses the issues related to overestimation of values. The fusion of laboratory measurements with computational analysis ensures a robust and reliable quantification of porosity and permeability in metamorphic rocks.

5.2. Evaluating anisotropy of physical properties in metamorphic rocks using the multiphase-field simulations – implications for fluid flow

In this study, we initially performed two-phase simulations using PACE3D framework considering void spaces as one phase, and the solid rock mass as the second phase. This simulation (Fig. 10) resulted in a high deviation from the laboratory measured permeability values. On the other hand, the inclusion of phyllosilicates as a third phase in the three-phase simulation has significantly improved the results. Several key factors contribute to this enhanced accuracy. The three-phase model accounting for the presence of phyllosilicates (Fig. 12), adds a more specific layer of anisotropy to the simulation; in real rocks, this geological structural distribution of layering/anisotropy is expected to influence fluid flow.

It may be noted that the similarity between permeability values in the three-phase simulations and laboratory measurements is obvious in Fig. 13 for all the schist samples except the one from 416 m depth. This implies that in the sample from 416 m depth, there may be other factors influencing the permeability apart from the presence of oriented phyllosilicates in the rock. We envisage that the microstructure of this sample is one of the critical factors. As mentioned in section 2, the sample from 416 m depth has layering defined by mica and quartz grains

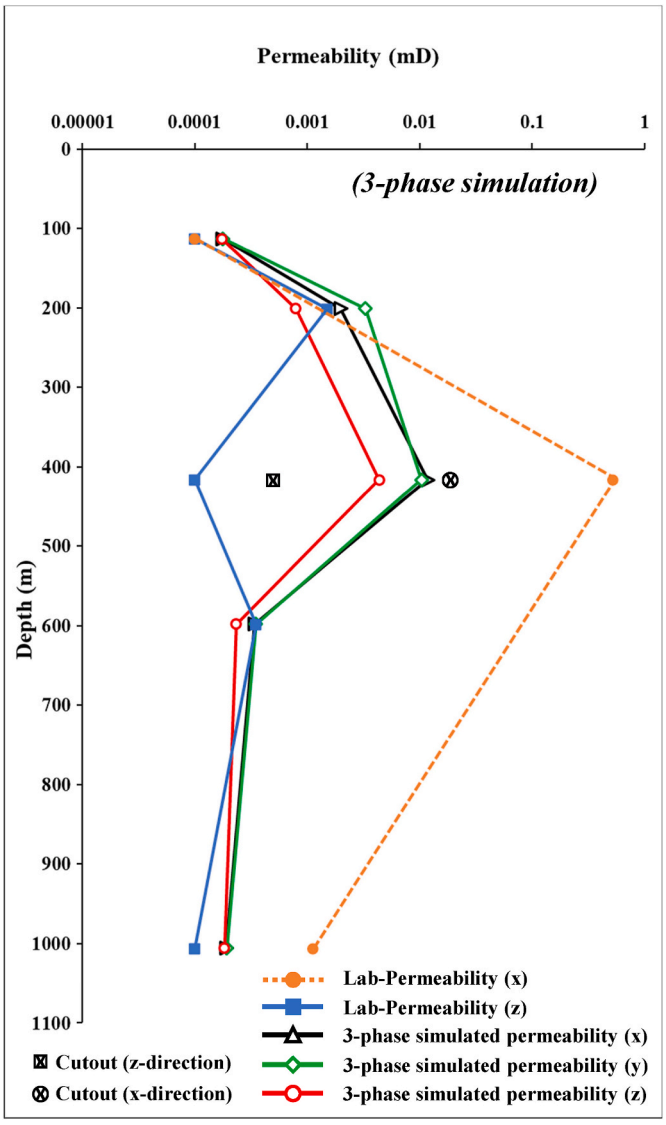

Figure-13. Depth vs. 3-phase simulated permeability graphs of the investigated schist samples. Compare with the 2-phase simulated permeability graphs for the same samples presented in Fig. 10. All simulations were done by applying PACE3D framework to µCT data in x, y and z directions. Laboratory permeability data are also plotted for comparison. The box and circle with a cross represent simulated 3-phase permeability values of small cutouts extracted from the µCT data of sample from 416 m depth from z- and x-directions, respectively. See text for discussion.

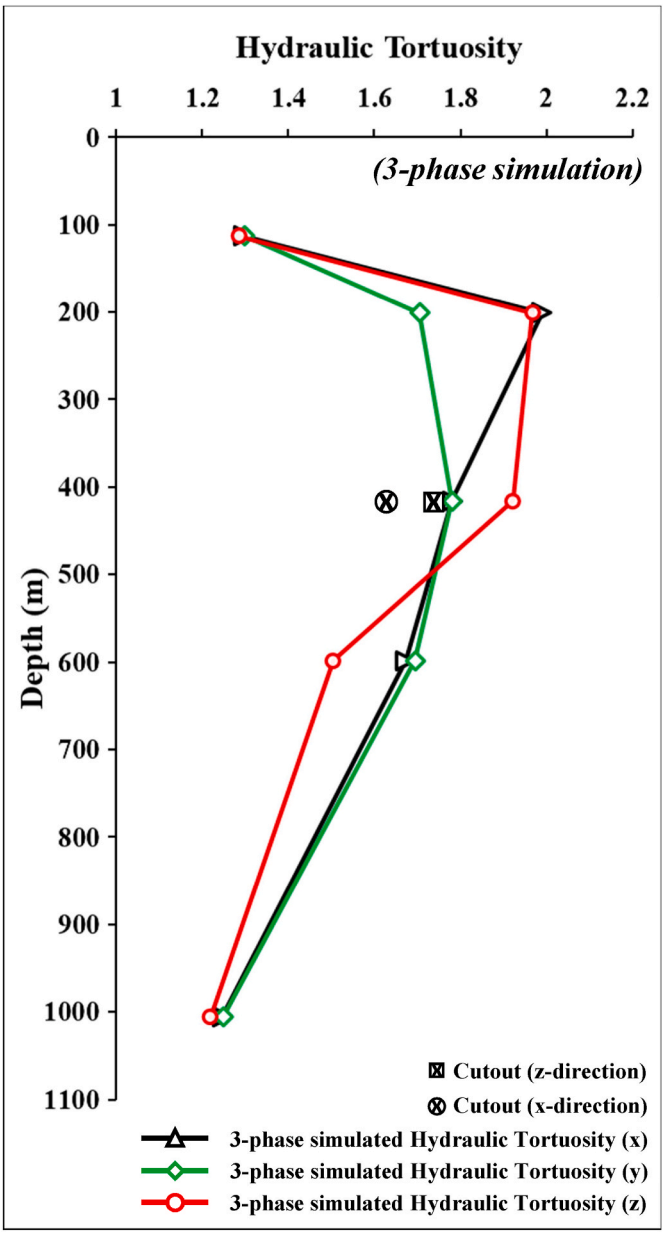

Figure-14. Depth vs. 3-phase simulated hydraulic tortuosity plots for the schist samples. The tortuosity was simulated by applying PACE3D framework to µCT data in three directions (x, y and z). The box and circle with a cross represent simulated 3-phase hydraulic tortuosity of small cutouts extracted from the µCT data of 416m depth sample from z- and x-directions, respectively.

of varying grain size, which incorporates an additional anisotropy to the system. The raw µCT data acquisition, which is done on the large NX size core (borehole sample) records this anisotropy, and is simulated using PACE3D framework (Fig. 13). However, the laboratory measurement of permeability is done in a small core extracted from the large borehole sample, which dominantly contained this grain-size layering anisotropy. Therefore, we hypothesize that the deviation in permeability between laboratory experiment and simulations maybe on account of the difference in the sample dimensions. In order to test this hypothesis, and better compare simulations with the laboratory measurements, we extracted two small cutouts (x- and z-directions) from µCT data; care was taken to extract the cutouts from the same position from where the small core was physically drilled in the laboratory. As shown in Fig. 13, this approach brings the simulated permeability of the cutouts closer to the laboratory measured values. However, still there is a visible deviation from the real values, which needs more detailed explanation and implies that the reason for this may be at the grain-scale not visible to the human eye.

The schist sample at 416 m depth exhibits a layered microstructure, as illustrated in Fig. 3c. This sample has different interfaces that induce anisotropy, marked as quartz-mica interface, quartz-quartz interface, mica-mica interface and also a sharp boundary between quartz-rich layer and phyllosilicate-rich layer (Fig. 15a). According to us, each of these interfaces is expected to contribute to permeability and its anisotropy to some extent, which requires microscale simulation. We generated a numerical polycrystalline microstructure to mimic these different interfaces – mica and quartz (Fig. 15b), mica-mica and quartz-quartz (Fig. 15c). It may be noted that the order parameter that represents two different grains within the numerical microstructure, decreases over the diffuse interface region along the grain boundary (green and teal coloured lines in the plot in Fig. 15b). Permeability modelling

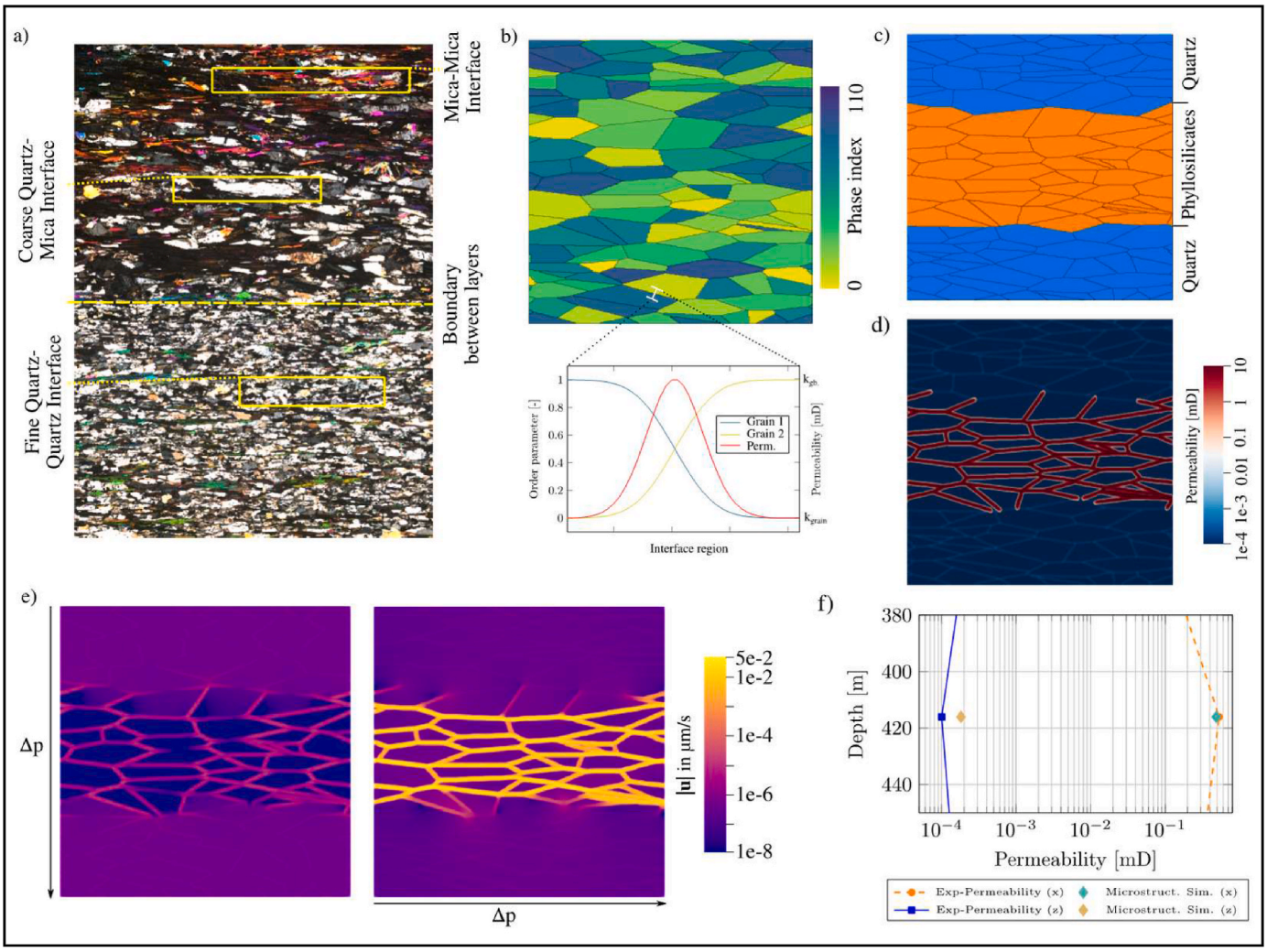

Figure-15. a) Layered microstructure in schist sample at 416 m depth with different mineral phase interfaces marked (see Fig. 3c). b) Numerical polycrystalline microstructure with stretched grains mimicking the natural rock in (a). The order parameter (representing grains) decreases over the diffuse interface region (green and teal coloured lines in the above plot), which enables the modelling of an increased permeability at the grain boundaries (red line in the plot). c) Quartz and Phyllosilicate layers in (b). d) Resulting modelled permeability in (b). The permeability is the highest at grain boundaries in the Phyllosilicate layer, increased at grain boundaries in the Quartz layer, and the lowest in the bulk grain region. e) Resulting fluid flow field |u|, when the flow is perpendicular (left) and parallel (right) to the layered rock. f) Computed effective permeability of fluid flow simulations compared to the laboratory measurements. (For interpretation of the references to colour in this figure legend, the reader is referred to the Web version of this article.)

using this setup in PACE3D shows increased permeability at grain boundaries (represented by red line in the plot in Fig. 15b). Permeability calculated at mica-mica and quartz-quartz interfaces is shown in Fig. 15d. Further the influence of this microstructure on directional variation in fluid flow parallel and perpendicular to the anisotropy is shown in Fig. 15e. Accordingly, it is observed (a) the quartz-quartz interface has lower permeability vis-à-vis mica-mica interface (Fig. 15d) (b) fluid flow field (|u| in µm/s in Fig. 15e) under an applied pressure gradient (Δp) is strong parallel to the layering (anisotropy) and weak perpendicular to it. Computed effective permeability (see section 3.4.2) for the cutouts has values much closer to the laboratory measured permeability (Fig. 15f). This establishes the role of the different mineral/phase interfaces in controlling permeability and its anisotropy, as hypothesized by us (above) is correct. This also indicates that permeability analysis from µCT data of large samples, which do not account for contributions from grain-interface properties, must be treated with caution. Our grain-scale simulations establish that permeability at grain interfaces are diffusive and variable for different phase boundaries. Permeability closest to the real values can be simulated only when all these aspects are factored into the computation.

This implies that the material properties of mineral grains constituting the metamorphic rocks are affected largely due to heterogeneity and strain variations, and therefore the permeability might actually be strongly increased along the grain boundaries in the metamorphic rocks. In future, the present simulation approach can even be further extended by explicitly incorporating the pores occurring at the grain boundaries to improve the prediction of the numerical simulations. This will also allow for conducting coupled mechanical and fluid-flow simulations to predict both the structural integrity and hydraulic characteristics, such as those encountered during hydrofracturing.

6. Conclusion

The present paper has brought to light the challenges that occur in the application of X-ray micro-CT (µCT) studies of schists vis-à-vis their petrophysical characterization. A *modus operandi* integrating laboratory measurement of porosity/permeability of the schists with µCT data and phase-field numerical simulation/modelling is developed; the latter takes into account 3-phase (voids + phyllosilicates + other minerals) simulations, which is not possible with most µCT post-processing

algorithms. This leads to proper petrophysical characterization of metamorphic rocks, and enhances the knowledge about the control of fabric anisotropy on permeability, thus having implications on fluid flow. The most important conclusions from our study are:

a) Most data processing of μCT images to calculate porosity is done considering pores/voids and rock mass as part of a two-phase (binary) system. This leads to inaccurate estimation of porosity (and other petrophysical properties) in metamorphic rocks such as schist investigated in the present study. This approach yielded a porosity value ranging between 5% – 6% and permeability of 10^5 D for our schist samples. These are abnormally high compared to the laboratory measured porosity values of 1%–2% and permeability in the range of 10^{-3} to 10^{-4} mD for the same schists. This implies that μCT data processing considering a binary system may have pitfalls and is not valid for metamorphic rocks like schists that are structurally anisotropic.
b) We conclude that laboratory measured values of porosity are important to fix the correct threshold of the greyscale CT images for processing permeability values. In our five schist samples, this yielded permeability ranging between 10^{-3} to 10^{-4} mD, which is similar to the laboratory permeability measured in the schists from different depths and justifies our approach. However, it is observed that there is a disparity between permeability values in the simulations and laboratory measurements in the sample from 416 m depth. This is attributed to other factors influencing the permeability, such as layered microstructure comprising various mineral-interfaces (quartz-mica, quartz-quartz and mica-mica) and sharp boundary between quartz-rich and phyllosilicate-rich layers. This necessitates a multiphase-field approach to evaluate role of rock microstructure on permeability and its anisotropy, and its influence on fluid flow.
c) We used a multiphase-field approach for numerical simulations by incorporating the PACE3D framework in our work which is crucial for computing effective permeability. This considers various mineral/phase interfaces which control the permeability and its anisotropy. Permeability at grain interfaces is taken into account in the grain-scale simulations. This involves considering diffusive permeability at grain boundaries and accounts for non-uniform permeability across different mineral grains/phases. Only when all of these factors are taken into account during computation, can permeability that is close to the real/laboratory values be simulated.

Since many metamorphic rocks are hosts to hydrothermal mineral deposits, understanding of relation between their fabric anisotropy, petrophysical properties, and fluid flow is important. We envisage that the approach adopted in this paper could be critical in future studies dealing with hydrothermal mineralization in metamorphic terrains.

CRediT authorship contribution statement

Ritwik Chakraborty: Writing – original draft, Methodology, Formal analysis, Data curation, Conceptualization. **Michael Späth:** Writing – review & editing, Writing – original draft, Formal analysis, Data curation. **Akash Kumar:** Writing – review & editing, Writing – original draft, Data curation. **Benjamin Busch:** Writing – review & editing, Methodology, Data curation. **Britta Nestler:** Writing – review & editing, Validation. **Manish A. Mamtani:** Writing – review & editing, Methodology, Conceptualization. **Christoph Hilgers:** Writing – review & editing, Validation.

Declaration of competing interest

The authors declare that they have no known competing financial interests or personal relationships that could have appeared to influence the work reported in this paper.

Acknowledgements

This work is part of doctoral studies being carried out by Ritwik Chakraborty (RC). A portion of this research work was carried out by RC during his visit to KIT Karlsruhe, Germany as a part of the collaborative project of M.A. Mamtani (IIT Kharagpur, India) and Agnes Kontny and Christoph Hilgers (KIT Karlsruhe, Germany) that has been funded by the Research Group Linkage Programme of the Alexander von Humboldt Foundation (Ref. 3.41–121501-IND-IP). Financial assistance from BRNS through project number 52/14/02/2019-BRNS is gratefully acknowledged. Thanks are due to IIT Kharagpur for supporting RC through Institute Senior Research Fellowship. B. Nestler, M. Späth and A. Kumar acknowledge Helmholtz Association for funding the research work within the program "MTET: 38.04.04". We acknowledge constructive reviews by two anonymous journal referees and editorial handling by Virginia Toy that significantly helped improve this manuscript. Data files related to this study will be made available on request by the authors.

Data availability

Data will be made available on request.

References

Aerden, D.G., Ruiz-Fuentes, A., 2020. X-ray computed micro-tomography of spiral garnets: a new test of how they form. J. Struct. Geol. 136, 104054. https://doi.org/10.1016/j.jsg.2020.104054.

Ankit, K., Urai, J.L., Nestler, B., 2015. Microstructural evolution in bitaxial crack-seal veins: a phase-field study. J. Geophys. Res. Solid Earth 120 (5), 3096–3118. https://doi.org/10.1002/2015JB011934.

Arif, M., Mahmoud, M., Zhang, Y., Iglauer, S., 2021. X-ray tomography imaging of shale microstructures: a review in the context of multiscale correlative imaging. Int. J. Coal Geol. 233, 103641. https://doi.org/10.1016/j.coal.2020.103641.

Bagde, M.N., 2000. An investigation into strength and porous properties of metamorphic rocks in the Himalayas: a case study. Geotech. Geol. Eng. 18, 209–219. https://doi.org/10.1023/A:1026518616345.

Baveye, P.C., Laba, M., Otten, W., Bouckaert, L., Sterpaio, P.D., Goswami, R.R., Grinev, D., Houston, A., Hu, Y., Liu, J., Mooney, S., Pajor, R., Sleutel, S., Tarquis, A., Wang, W., Wei, Q., Sezgin, M., 2010. Observer-dependent variability of the thresholding step in the quantitative analysis of soil images and X-ray microtomography data. Geoderma 157 (1–2), 51–63. https://doi.org/10.1016/j.geoderma.2010.03.015.

Becker, I., Busch, B., Koehrer, B., Adelmann, D., Hilgers, C., 2019. Reservoir quality evolution of upper Carboniferous (Westphalian) tight gas sandstones, Lower Saxony Basin, NW Germany. J. Petrol. Geol. 42 (4), 371–392. https://doi.org/10.1111/jpg.12742.

Bhanot, K.K., Downes, H., Petrone, C.M., Humphreys-Williams, E., 2017. Textures in spinel peridotite mantle xenoliths using micro-CT scanning: examples from Canary Islands and France. Lithos 276, 90–102. https://doi.org/10.1016/j.lithos.2016.08.004.

Bloise, A., Ricchiuti, C., Lanzafame, G., Punturo, R., 2020. X-ray synchrotron microtomography: a new technique for characterizing chrysotile asbestos. Sci. Total Environ. 703, 135675. https://doi.org/10.1016/j.scitotenv.2019.135675.

Busch, A., Schweinar, K., Kampman, N., Coorn, A.B., Pipich, V., Feoktystov, A., Leu, L., Amann-Hildenbrand, A., Bertier, P., 2017. Determining the porosity of mudrocks using methodological pluralism. Geol. Soc. London, Special Pub. 454 (1), 15–38. https://doi.org/10.1144/SP454.1.

Callow, B., Falcon-Suarez, I., Marin-Moreno, H., Bull, J.M., Ahmed, S., 2020. Optimal X-ray micro-CT image based methods for porosity and permeability quantification in heterogeneous sandstones. Geophys. J. Int. 223 (2), 1210–1229. https://doi.org/10.1093/gji/ggaa321.

Cant, J.L., Siratovich, P.A., Cole, J.W., Villeneuve, M.C., Kennedy, B.M., 2018. Matrix permeability of reservoir rocks, Ngatamariki geothermal field, Taupo Volcanic Zone, New Zealand. Geoth. Energy 6, 1–28. https://doi.org/10.1186/s40517-017-0088-6.

Cappuccio, F., Toy, V.G., Mills, S., Adam, L., 2020. Three-dimensional separation and characterization of fractures in X-ray computed tomographic images of rocks. Front. Earth Sci. 8, 529263. https://doi.org/10.3389/feart.2020.529263.

Cárdenes, V., Merinero, R., De Boever, W., Rubio-Ordóñez, Á., Dewanckele, J., Cnudde, J.P., Boone, M., Hoorebeke, L.V., Cnudde, V., 2016. Characterization of micropyrite populations in low-grade metamorphic slate: a study using high-

*R*resolution X-ray tomography. Palaeogeogr. Palaeoclimatol. Palaeoecol. 441, 924–935. https://doi.org/10.1016/j.palaeo.2015.10.044.

Cárdenes Van den Eynde, V., Cnudde, V., De Boever, W., Mateos, F.J., 2013. Micro-CT and mercury intrusion porosimetry characterization of the fabric of roofing slate. In: 1st International Conference on Tomography of Materials and Structures (ICTMS 2013), pp. 225–228. http://hdl.handle.net/1854/LU-4178440.

Chakraborty, R., Mamtani, M.A., Tripathi, S., Singh, A., Rakesh, S., Chakrabarti, K., Sinha, D.K., 2022. Variation in anisotropy of magnetic susceptibility with depth in the upper 1 km of the earth's crust in Singhbhum region (India)—first results. J. Geol. Soc. India 98 (12), 1665–1670. https://doi.org/10.1007/s12594-022-2235-3.

Cnudde, V., Boone, M.N., 2013. High-resolution X-ray computed tomography in geosciences: a review of the current technology and applications. Earth Sci. Rev. 123, 1–17. https://doi.org/10.1016/j.earscirev.2013.04.003.

Corti, L., Zucali, M., Visalli, R., Mancini, L., Sayab, M., 2019. Integrating X-ray computed tomography with chemical imaging to quantify mineral re-crystallization from granulite to eclogite metamorphism in the Western Italian Alps (Sesia-Lanzo Zone). Front. Earth Sci. 7, 327. https://doi.org/10.3389/feart.2019.00327.

Denison, C., Carlson, W., Ketcham, R.A., 1997. Three-dimensional quantitative textural analysis of metamorphic rocks using high-resolution computed X-ray tomography: Part I. Methods and techniques. J. Metamorph. Geol. 15, 29–44. https://doi.org/10.1111/j.1525-1314.1997.00006.x.

Dinda, S.K., Jana, S., Roy, G.G., Srirangam, P., 2019. Effect of beam oscillation on porosity and intermetallics of electron beam welded DP600-steel to Al 5754-alloy. J. Mater. Process. Technol. 265, 191–200. https://doi.org/10.1016/j.jmatprotec.2018.10.026.

Dipple, G.M., Bons, P., Oliver, N.H.S., 2005. A vector of high-temperature paleo-fluid flow deduced from mass transfer across permeability barriers (quartz veins). Geofluids 5 (2), 67–82. https://doi.org/10.1111/j.1468-8123.2005.00099.x.

Faulkner, D.R., Rutter, E.H., 2001. Can the maintenance of overpressured fluids in large strike-slip fault zones explain their apparent weakness? Geology 29 (6), 503–506. https://doi.org/10.1130/0091-7613(2001)029<0503:CTMOOF>2.0.CO;2.

Fogden, A., McKay, T., Turner, M., Marathe, R., Senden, T., 2014. Micro-CT analysis of pores and organics in unconventionals using novel contrast strategies. In: Unconventional Resources Technology Conference. Society of Exploration Geophysicists, American Association of Petroleum Geologists, Society of Petroleum Engineers, Denver, Colorado, pp. 960–969. https://doi.org/10.15530/urtec-2014-1922195.

Galindo, K., Lins, C., Guimarães, L., Lima, A., Silva, K., Nova, A., 2022. Application of microtomography and petrography techniques for the characterization of porosity of synthetic carbonatic rock minerals before and after acidification processes. Sci. Rep. 12 (1), 17026. https://doi.org/10.1038/s41598-022-19577-8.

Ganzhorn, A.C., Pilorgé, H., Reynard, B., 2019. Porosity of metamorphic rocks and fluid migration within subduction interfaces. Earth Planet Sci. Lett. 522, 107–117. https://doi.org/10.1016/j.epsl.2019.06.030.

Garum, M., Glover, P.W., Lorinczi, P., Drummond-Brydson, R., Hassanpour, A., 2020. Micro-and nano-scale pore structure in gas shale using Xμ-CT and FIB-SEM techniques. Energy Fuel. 34 (10), 12340–12353. https://doi.org/10.1021/acs.energyfuels.0c02025.

Ghosh, S.K., Sengupta, S., 1987. Progressive development of structures in a ductile shear zone. J. Struct. Geol. 9 (3), 277–287. https://doi.org/10.1016/0191-8141(87)90052-6.

Giamas, V., Koutsovitis, P., Sideridis, A., Turberg, P., Grammatikopoulos, T.A., Petrounias, P., Giannakopoulou, P.P., Koukouzas, N., Hatzipanagiotou, K., 2022. Effectiveness of X-ray micro-CT applications upon mafic and ultramafic ophiolitic rocks. Micron 158, 103292. https://doi.org/10.1016/j.micron.2022.103292.

Hötzer, J., Reiter, A., Hierl, H., Steinmetz, P., Selzer, M., Nestler, B., 2018. The parallel multi-physics phase-field framework Pace3D. J. Comput. Sci. 26, 1–12. https://doi.org/10.1016/j.jocs.2018.02.011.

Huang, X., Yang, D., Kang, Z., 2021. Three-phase segmentation method for organic matter recognition in source rocks via CT images: a case study on oil shale pyrolyzed by steam. Energy Fuel. 35 (12), 10075–10085. https://doi.org/10.1021/acs.energyfuels.1c00917.

Ketcham, R.A., 2005. Three-dimensional grain fabric measurements using high-resolution X-ray computed tomography. J. Struct. Geol. 27 (7), 1217–1228. https://doi.org/10.1016/j.jsg.2005.02.006.

Klinkenberg, L.J., 1941. The permeability of porous media to liquids and gases. Drilling and Production Practice. American Petroleum Institute, pp. 200–213.

Kranz, R.L., Frankel, A.D., Engelder, T., Scholz, C.H., 1979. The permeability of whole and jointed Barre granite. Int. J. Rock Mech. Min. Sci. Geomech. Abstracts 16 (4), 225–234. https://doi.org/10.1016/0148-9062(79)91197-5.

Kristensen, L., Hjuler, M.L., Frykman, P., Olivarius, M., Weibel, R., Nielsen, L.H., Mathiesen, A., 2016. Pre-drilling assessments of average porosity and permeability in the geothermal reservoirs of the Danish area. Geoth. Energy 4, 1–27. https://doi.org/10.1186/s40517-016-0048-6.

Kumar, A., Prajapati, N., Späth, M., Busch, B., Schneider, D., Hilgers, C., Nestler, B., 2023. Qualitative dissolution modeling of etch-pit formation on the K-feldspar surface through phase-field approach. J. Geophys. Res. Solid Earth 128 (4), e2022JB025749. https://doi.org/10.1029/2022JB025749.

Laubach, S.E., Lander, R.H., Criscenti, L.J., Anovitz, L.M., Urai, J.L., Pollyea, R.M., Hooker, J.M., Narr, W., Evans, M.A., Kerisit, S.N., Olson, J.E., Dewers, T., Fisher, D., Bodnar, R., Evans, B., Dove, P., Bonnell, L.M., Marder, M.P., Pyrak-Nolte, L., 2019. The role of chemistry in fracture pattern development and opportunities to advance interpretations of geological materials. Rev. Geophys. 57 (3), 1065–1111. https://doi.org/10.1029/2019RG000671.

Leclere, H., Buatier, M., Charpentier, D., Sizun, J.P., Labaume, P., Cavailhes, T., 2012. Formation of phyllosilicates in a fault zone affecting deeply buried arkosic sandstones: their influence on petrophysic properties (Annot sandstones, French external Alps). Swiss J. Geosci. 105 (2), 299–312. https://doi.org/10.1007/s00015-012-0099-z.

Liu, Q., Sun, M., Sun, X., Liu, B., Ostadhassan, M., Huang, W., Chen, X., Pan, Z., 2023. Pore network characterization of shale reservoirs through state-of-the-art X-ray computed tomography: a review. Gas Sci. Eng. 204967. https://doi.org/10.1016/j.jgsce.2023.204967.

Mamtani, M.A., Pal, T., Greiling, R.O., 2013. Kinematic analysis using AMS data from a deformed granitoid. J. Struct. Geol. 50, 119–132. https://doi.org/10.1016/j.jsg.2012.03.002.

Maniscalco, R., Fazio, E., Punturo, R., Cirrincione, R., Di Stefano, A., Distefano, S., Forzese, M., Lanzafame, G., Leonardi, G.S., Montalbano, S., Pellegrino, A.G., Raele, A., Palmeri, G., 2022. The porosity in heterogeneous carbonate reservoir rocks: tectonic versus diagenetic imprint—a multi-scale study from the hyblean plateau (SE sicily, Italy). Geosciences 12 (4), 149. https://doi.org/10.3390/geosciences12040149.

Maurício, A., Pereira, M.F., Rocha, C., Figueiredo, C., Marques, J.M., 2017. X-ray micro-CT study of Cabeço De Vide serpentinites and carbonate rock samples: a preliminary approach. Procedia Earth Planet. Sci. 17, 952–955. https://doi.org/10.1016/j.proeps.2017.01.034.

Mayo, S., Josh, M., Nesterets, Y., Esteban, L., Pervukhina, M., Clennell, M.B., Maksimenko, A., Hall, C., 2015. Quantitative micro-porosity characterization using synchrotron micro-CT and xenon K-edge subtraction in sandstones, carbonates, shales and coal. Fuel 154, 167–173. https://doi.org/10.1016/j.fuel.2015.03.046.

McKeag, S.A., Craw, D., Norris, R.J., 1989. Origin and deposition of a graphitic schist-hosted metamorphogenic Au-W deposit, Macraes, East Otago, New Zealand. Miner. Deposita 24, 124–131. https://doi.org/10.1007/BF00206316.

Mees, F., Swennen, R., Geet, M.V., Jacobs, P., 2003. Applications of X-ray computed tomography in the geosciences. Geol. Soc. London, Special Pub. 215 (1), 1–6. https://doi.org/10.1144/GSL.SP.2003.215.01.01.

Monsees, A.C., Busch, B., Hilgers, C., 2021. Compaction control on diagenesis and reservoir quality development in red bed sandstones: a case study of Permian Rotliegend sandstones. Int. J. Earth Sci. 110 (5), 1683–1711. https://doi.org/10.1007/s00531-021-02036-6.

Monsees, A.C., Subhedar, A., Busch, B., Nestler, B., Hilgers, C., 2020. Calibrating micro-computed tomography data to permeability experiments and petrography–insights from Digital Rocks. Oil Gas (3/2020), 28. https://doi.org/10.5445/IR/1000123827.

Pal, D.C., Banerjee, A., Dutta, A., Sarangi, A.K., 2022. Hydrothermal alterations and U-REE mineralisation in the Narwapahar uranium deposit, Singhbhum shear zone, India. J. Earth Syst. Sci. 131 (1), 31. https://doi.org/10.1007/s12040-021-01782-0.

Passchier, C.W., Trouw, R.A., 2005. Microtectonics. Springer Science & Business Media.

Prajapati, N., Abad Gonzalez, A., Selzer, M., Nestler, B., Busch, B., Hilgers, C., 2020. Quartz cementation in polycrystalline sandstone: insights from phase-field simulations. J. Geophys. Res. Solid Earth 125 (2), e2019JB019137. https://doi.org/10.1029/2019JB019137.

Prajapati, N., Selzer, M., Nestler, B., 2017. Computational modeling of calcite cementation in saline limestone aquifers: a phase-field study. Geoth. Energy 5 (1), 1–18. https://doi.org/10.1186/s40517-017-0072-1.

Punturo, R., Indelicato, V., Lanzafame, G., Maniscalco, R., Fazio, E., Bloise, A., Muschella, L., Cirrincione, R., 2023. Petrographic, microstructural and petrophysical study of asphaltic limestone employed in the Late Baroque towns of the Val di Noto UNESCO site (south-eastern Sicily). Construct. Build. Mater. 371, 130730. https://doi.org/10.1016/j.conbuildmat.2023.130730.

Radhakrishna, B.P., Curtis, L.C., 1999. Gold in India. GSI Pub. 3 (1).

Ramos, M.J., Espinoza, D.N., Goldfarb, E.J., Tisato, N., Laubach, S.E., Torres-Verdín, C., 2019. Microstructural controls on elastic anisotropy of finely laminated Mancos Shale. Geophys. J. Int. 216 (2), 991–1004. https://doi.org/10.1093/gji/ggy474.

Sadeghnejad, S., Reinhardt, M., Enzmann, F., Arnold, P., Brandstätter, B., Ott, H., Wilde, F., Hupfer, S., Schäfer, T., Kersten, M., 2023. Minkowski functional evaluation of representative elementary volume of rock microtomography images at multiple resolutions. Adv. Water Resour. 179, 104501. https://doi.org/10.1016/j.advwatres.2023.104501.

Saha, A.K., 1994. Crustal evolution of singhbhum–North Orissa, eastern India. J. Geol. Soc. India Memoir 27, 341.

Saraf, S., Bera, A., 2021. A review on pore-scale modeling and CT scan technique to characterize the trapped carbon dioxide in impermeable reservoir rocks during sequestration. Renew. Sustain. Energy Rev. 144, 110986. https://doi.org/10.1016/j.rser.2021.110986.

Späth, M., Nestler, N., 2023. Permeability evolution in open fractures during precipitation and dissolution - a phase-field study. Adv. Water Resour. 182, 104563. https://doi.org/10.1016/j.advwatres.2023.104563.

Späth, M., Selzer, M., Busch, B., Schneider, D., Hilgers, C., Urai, J.L., Nestler, B., 2023. Phase-field simulations of epitaxial crystal growth in open fractures with reactive lateral flow. Water Resour. Res. 59 (8), e2023WR034605. https://doi.org/10.1029/2023WR034605.

Späth, M., Spruženiece, L., Urai, J.L., Selzer, M., Arndt, M., Nestler, B., 2021. Kinematics of crystal growth in single-seal syntaxial veins in limestone-A phase-field study. J. Geophys. Res. Solid Earth 126 (10), e2021JB022106. https://doi.org/10.1029/2021JB022106.

Späth, M., Urai, J.L., Nestler, B., 2022a. Formation of radiator structures in quartz veins - phase-field modeling of multi-crack sealing. J. Struct. Geol. 158, 104576. https://doi.org/10.1016/j.jsg.2022.104576.

Späth, M., Urai, J.L., Nestler, B., 2022b. Incomplete crack sealing causes localization of fracturing in hydrothermal quartz veins. Geophys. Res. Lett. 49 (15), e2022GL098643. https://doi.org/10.1029/2022GL098643.
Steinbach, I., Pezzolla, F., Nestler, B., Seeßelberg, M., Prieler, R., Schmitz, G.J., Rezende, J.L., 1996. A phase field concept for multiphase systems. Phys. Nonlinear Phenom. 94 (3), 135–147. https://doi.org/10.1016/0167-2789(95)00298-7.
Vishnu, C.S., Lahiri, S., Mamtani, M.A., 2018. The relationship between magnetic anisotropy, rock-strength anisotropy and vein emplacement in gold-bearing metabasalts of Gadag (South India). Tectonophysics 722, 286–298. https://doi.org/10.1016/j.tecto.2017.09.011.
Voltolini, M., Zandomeneghi, D., Mancini, L., Polacci, M., 2011. Texture analysis of volcanic rock samples: quantitative study of crystals and vesicles shape preferred orientation from X-ray microtomography data. J. Volcanol. Geoth. Res. 202 (1–2), 83–95. https://doi.org/10.1016/j.jvolgeores.2011.02.003.
Wang, K., Ma, L., Taylor, K.G., 2023. Microstructure changes as a response to CO2 storage in sedimentary rocks: recent developments and future challenges. Fuel 333, 126403. https://doi.org/10.1016/j.fuel.2022.126403.
Wennberg, O.P., Rennan, L., 2018. A brief introduction to the use of X-ray computed tomography (CT) for analysis of natural deformation structures in reservoir rocks. Geol. Soc. London, Special Pub. 459 (1), 101–120. https://doi.org/10.1144/SP459.10.
Yang, B., Wang, H., Wang, B., Shen, Z., Zheng, Y., Jia, Z., Yan, W., 2021. Digital quantification of fracture in full-scale rock using micro-CT images: a fracturing experiment with N2 and CO2. J. Petrol. Sci. Eng. 196, 107682. https://doi.org/10.1016/j.petrol.2020.107682.
Zambrano, M., Tondi, E., Mancini, L., Arzilli, F., Lanzafame, G., Materazzi, M., Torrieri, S., 2017. 3D Pore-network quantitative analysis in deformed carbonate grainstones. Mar. Petrol. Geol. 82, 251–264. https://doi.org/10.1016/j.marpetgeo.2017.02.001.
Zambrano, M., Tondi, E., Mancini, L., Lanzafame, G., Trias, F.X., Arzilli, F., Materazzi, M., Torrieri, S., 2018. Fluid flow simulation and permeability computation in deformed porous carbonate grainstones. Adv. Water Resour. 115, 95–111. https://doi.org/10.1016/j.advwatres.2018.02.016.
Zeng, Z., Shan, X., Hao, G., He, W., Zheng, C., Yi, J., Guo, J., 2022. Semiquantitative microscopic pore characterizations of the metamorphic rock reservoir in the central paleo-uplift belt, Songliao Basin. Sci. Rep. 12 (1), 2606. https://doi.org/10.1038/s41598-022-05960-y.
Zhao, Y., He, X., Jiang, L., Wang, Z., Ning, J., Sainoki, A., 2023. Influence analysis of complex crack geometric parameters on mechanical properties of soft rock. Int. J. Coal Sci. Technol. 10 (1), 1–15. https://doi.org/10.1007/s40789-023-00649-7.
Zhuang, L., Shin, H.S., Yeom, S., Pham, C.N., Kim, Y.J., 2022. A novel method for estimating subresolution porosity from CT images and its application to homogeneity evaluation of porous media. Sci. Rep. 12 (1), 16229. https://doi.org/10.1038/s41598-022-20086-x.